University of Alberta

Low Energy (K^+, ^{12}C) Charge Exchange Cross Section Measurements

by

Hui-Siong Ng

A thesis submitted to the Faculty of Graduate Studies and Research in partial fulfillment of the requirements for the degree of **Master of Science**.

Department of Physics

Edmonton, Alberta

Spring 2000

National Library of Canada
Acquisitions and Bibliographic Services
395 Wellington Street
Ottawa ON K1A 0N4
Canada

Bibliothèque nationale du Canada
Acquisitions et services bibliographiques
395, rue Wellington
Ottawa ON K1A 0N4
Canada

Your file Votre référence

Our file Notre référence

The author has granted a non-exclusive licence allowing the National Library of Canada to reproduce, loan, distribute or sell copies of this thesis in microform, paper or electronic formats.

L'auteur a accordé une licence non exclusive permettant à la Bibliothèque nationale du Canada de reproduire, prêter, distribuer ou vendre des copies de cette thèse sous la forme de microfiche/film, de reproduction sur papier ou sur format électronique.

The author retains ownership of the copyright in this thesis. Neither the thesis nor substantial extracts from it may be printed or otherwise reproduced without the author's permission.

L'auteur conserve la propriété du droit d'auteur qui protège cette thèse. Ni la thèse ni des extraits substantiels de celle-ci ne doivent être imprimés ou autrement reproduits sans son autorisation.

0-612-60159-5

Canada

University of Alberta

Library Release Form

Name of Author: Hui-Siong Ng

Title of Thesis: Low Energy (K^+, ^{12}C) Charge Exchange Cross Section Measurements

Degree: Master of Science

Year this Degree Granted: 2000

Permission is hereby granted to the University of Alberta Library to reproduce single copies of this thesis and to lend or sell such copies for private, scholarly or scientific research purposes only.

The author reserves all other publication and other rights in association with the copyright in the thesis, and except as hereinbefore provided, neither the thesis nor any substantial portion thereof may be printed or otherwise reproduced in any material form whatever without the author's prior written permission.

Hui-Siong Ng
CSR 201
University of Alberta
Edmonton, AB
Canada, T6G 2G6

Date: 19 Jan 2000

University of Alberta

Faculty of Graduate Studies and Research

The undersigned certify that they have read, and recommend to the Faculty of Graduate Studies and Research for acceptance, a thesis entitled **Low Energy (K^+, ^{12}C) Charge Exchange Cross Section Measurements** submitted by Hui-Siong Ng in partial fulfillment of the requirements for the degree of **Master of Science**.

P. Kitching

J. Pinfold

F. Khanna

M. de Montigny

Date: 19/1/2000

Abstract

K^+ charge exchanging (CEX) with the ^{12}C in the target introduces background for the E787 rare decay $K^+ \to \pi^+\nu\bar{\nu}$ search. No cross section measurement was ever performed below 100 MeV. By installing a trigger to detect the $K^0_S \to \pi^+\pi^-$ decay resulting from CEX, E787 has been able to measure first-hand the total CEX cross section at energies below 100 MeV. The cross section is found to be flat at 16.1±1.3 mb for energies between 40 and 100 MeV. The cross section gradually drops off to 6±0.6 mb at threshold. This 6 mb can be attributed to resolution effect. Contribution from other systematic errors is around 20%. There are definite disagreements between this result and those from optical model calculations. The discrepancies could be resolved if the detector resolution effect is properly accounted for in the experimental measurement.

Acknowledgements

The work for this thesis would not have been completed without the help of many individuals listed below:

I would like to thank my supervisor Peter Kitching for his immense patience despite the lack of progress during the experiment runtime in 1998. Especially thankful to D. Bryman, A. Konaka, T. Numao, J. Mildenberger, and G. Redlinger for the many suggestions and discussions regarding the detector and the analysis. Not to forget the grocery shopping ride they had to provide during the 1998 run to avert my starvation. Thanks also to the collaborators at BNL, KEK, and Princeton. Especially want to mention Steve Adler and Chi Ng for providing the "unnecessary" diversions in forms of Linux computing that made the stay at BNL extremely tolerable.

Finally, I would like to thank my parents for allowing me to fool around with physics even though they think that such work seems impractical to a layperson.

Preface

The following analysis procedures were taken directly from the standard $\pi^+\nu\bar{\nu}$ analysis:

- Selection cuts for $K_{\mu 2}$ and piscat events
- Procedure for A_{k_s} Measurement
- $K_{\mu 2}$ acceptance measurement

Aside from those items, all the analysis works were performed by the author. The author also spent 9 months at Brookhaven National Lab in 1998 during the E787 experimental run to assist in the data taking. Duties assigned during that period included RS energy calibration, CCD and UTC maintainance.

Contents

Bibliography 4

1 Introduction 1
- 1.1 Theoretical Motivation for E787 . . . 1
- 1.2 CEX Background . . . 3

2 Theory 6
- 2.1 Kaon-Nucleon Interaction . . . 6
- 2.2 Kaon-Nucleus Interaction . . . 8
- 2.3 Optical Model . . . 10

3 The E787 Detector 12
- 3.1 Detector Description . . . 12
  - 3.1.1 Beam . . . 13
  - 3.1.2 Target . . . 13
  - 3.1.3 Drift Chamber . . . 15
  - 3.1.4 Range Stack . . . 15
  - 3.1.5 Photon Veto . . . 16
- 3.2 CEX Signal in the E787 Detector . . . 16
- 3.3 The CEX Trigger . . . 17
- 3.4 CEX Data . . . 18

4 Offline Analysis 19
- 4.1 Event Reconstruction . . . 19
- 4.2 Interaction Energy . . . 24
  - 4.2.1 B4 Energy Calibration . . . 24
  - 4.2.2 Systematic Uncertainty of Energy Measurement . . . 27
- 4.3 Events Selection . . . 32

4.3.1 Backgrounds 32
4.3.2 Basic Topology Cuts 40
4.3.3 Target Cuts 41
4.3.4 Kinematic Cuts 42
4.3.5 CEX Spectrum 43

5 Acceptance Measurement **49**
5.1 UMC based Measurement 50
5.1.1 Trigger Acceptance, A_{trig} 50
5.1.2 Target z correction, A_{tgz} 51
5.2 Data based Measurements 57
5.2.1 Cuts' Corrections 57
5.2.2 $\overline{\text{DELCO}}$ acceptance, A_{dc} 57
5.2.3 Nuclear Interaction Corrections 58
5.2.4 K^0_S Detection and Reconstruction Efficiency 60
5.2.5 Online PV Acceptance 61
5.2.6 Target Interaction Correction 65

6 Kaon Flux Normalization **69**
6.1 Kaon Transport Code 71
6.2 f_s Calculation 75

7 Conclusions **79**
7.1 Cross-Section Calculation 79
7.2 Systematic Errors 80
7.2.1 Energy Binning Effect 80
7.2.2 Energy Shifting 80
7.2.3 Kaon Scattering 81
7.3 Discussion 81
7.4 The Future 85

A UMC Performance **88**

List of Figures

1.1 CKM triangle determination from the K and B systems 2

2.1 The K^+p total cross section data 7
2.2 Measured values of R_T compared with different models prediction . . 9
2.3 Total CEX cross section based on optical model calculation 11

3.1 Schematic for the E787 detector 12
3.2 Endview of the target 14
3.3 Sideview of the target 14
3.4 The E787 Drift Chamber 15

4.1 An example of a reconstructed charge exchange event 22
4.2 Close up view of the Target Reconstruction 23
4.3 Close up view of the range stack track 23
4.4 Range, energy, and momentum distribution for $K_{\mu 2}$ after selection cuts 26
4.5 **B4ABM2** distribution for $K_{\mu 2}$ after selection cuts 27
4.6 Calibration curve for **B4ABM2** and **Ek** 28
4.7 **Ek** distributions at different kaon energy regimes 29
4.8 Proton energy spectrum from CEX interaction 31
4.9 Mass and momentum spectrum for events surviving the basic topology cuts 33
4.10 Mass and momentum spectrum for events surviving all cuts 34
4.11 K^0_S mass spectrum before and after cuts 35
4.12 A $K_{\pi 2}$ background event 37
4.13 Mass and momentum distribution for the ++ track 38
4.14 Removal of $K_{\pi 2}$ background using PIMASS and target cuts 44
4.15 Scatterplots of UMC data before and after cuts 45

4.16 CEX event distribution for the two hypotheses at different interaction energy 46
4.17 Opening angles between the $\pi^+\pi^-$ tracks for each interaction energy . 47
4.18 Stopping position of CEX kaon in the target 48

5.1 Kaon stopping distribution with zero beam offset 52
5.2 Kaon stopping distribution with offset = +10 cm 53
5.3 Kaon stopping distribution with offset = -10 cm 54
5.4 IC acceptance as a function of tgz 56
5.5 Schematic diagram on the K^0_S efficiency measurement 62
5.6 Detection efficiency for π^+ and π^- from the K^0_S and UMC data . . . 63
5.7 K^0_S reconstruction efficiency as a function of its momentum 64
5.8 Online Photon Veto efficiency 66
5.9 Pathlength of π^- in target 67
5.10 Experimental values of π^- total cross section with carbon 68

6.1 Schematic on the transport code of K^+ in the target 72
6.2 Two Pion energy loss in the target 74
6.3 Target z-energy distribution for $K_{\mu 2}$ 75
6.4 Target range-energy grid of CEX events 76

7.1 Experimental CEX cross section values 82
7.2 Cross section values for the systematic error studies 83

A.1 Comparison of RS range distributions of π^- at momenta 150, 230, 270 MeV/c between UMC and data 89
A.2 Comparison of RS range distributions of π^+ at momenta 150, 230, 270 MeV/c between UMC and data 90

List of Tables

1.1 Main Decay Modes of K_S^0 and K_L^0 4

4.1 A list of kaon decay modes as possible background in CEX 32
4.2 Acceptance for the possible background 39

5.1 CEX trigger acceptance factors 51
5.2 CEX event selection factor, A_{cex} 57
5.3 Target cut acceptance factor, A_{tt} 57
5.4 Online Delayed Coincidence Acceptance, A_{dc} 58
5.5 K_S^0 detection factor, A_{K_s} 61
5.6 PV acceptance factor, A_{PV} 65
5.7 Target nuclear interaction correction factor 68

6.1 Target thickness x used in cross-section calculation for each energy bin 71
6.2 $K_{\mu 2}$ event selection for 1997 runs with 670 MeV/c momentum 71
6.3 Trigger and COS3D acceptance factor for $K_{\mu 2}$ from UMC 76
6.4 Acceptance of the reconstruction cuts 77
6.5 Kaon flux normalization factor, f_s, at each energy 77

7.1 CEX cross-section for the proton and no-proton hypotheses 79
7.2 CEX cross-section for a 40 MeV bin size 80
7.3 CEX cross-section values for a 10 MeV bin size 80
7.4 CEX cross-section with different kaon threshold energy 81
7.5 List of systematic errors and their contribution to the cross section values 81

Chapter 1

Introduction

The E787 experiment at Brookhaven National Laboratory (BNL) is designed to search for the rare kaon decay, $K^+ \to \pi^+\nu\bar{\nu}$ (henceforth referred to as $\pi^+\nu\bar{\nu}$). Since its conception in 1983, the detector had undergone several upgrades to improve its sensitivity. Results from the 1995-1997 data produced a single $\pi^+\nu\bar{\nu}$ event observation, yielding a branching ratio of $1.5^{+3.4}_{-1.2} \times 10^{-10}$ [1]; a result that agrees with the Standard Model (SM) prediction.

Definitive measurement of such a low branching ratio requires suppression of all backgrounds to well below the sensitivity for the signal and reliable estimates of the residual background levels. This thesis will attempt to shed some light in understanding one of the least certain backgrounds in the E787 experiment, namely the low energy kaon charge exchange (CEX) background.

1.1 Theoretical Motivation for E787

The decay $K^+ \to \pi^+\nu\bar{\nu}$, a flavor changing neutral current process, is a highly suppressed second order weak decay. The presence of the top quark in the loops makes this decay very sensitive to $|V_{td}|$, the coupling of the top and down quarks in the CKM matrix. The branching ratio calculation for this decay is relatively clean theoretically. Hadronic uncertainties are removed by normalizing to the branching ratio of $K^+ \to \pi^0 e^+ \nu_e$. After a next-to-leading order-logarithmic analysis of QCD effects and calculations of two-electroweak-loop effects, the intrinsic uncertainty is only about 7% [5, 6, 7, 8].

Long distance contributions to the branching ratio (*i.e.* meson, photon exchanges) are found to be negligible [9, 10]. This implies that not only can the effects of the

SM short-distance physics be clearly discerned in this process, but also the effects of possible non-SM physics. The non-SM physics signature of $K^+ \to \pi^+$'nothing' includes $K^+ \to \pi^+ \nu\bar{\nu}$ with non-SM intermediate states (such as virtual supersymmteric particles), $K^+ \to \pi^+ X^0 X^{0\prime}$ where X^0 and $X^{0\prime}$ are not neutrinos, and $K^+ \to \pi^+ X^0$ where X^0 is a single, non-interacting particle.

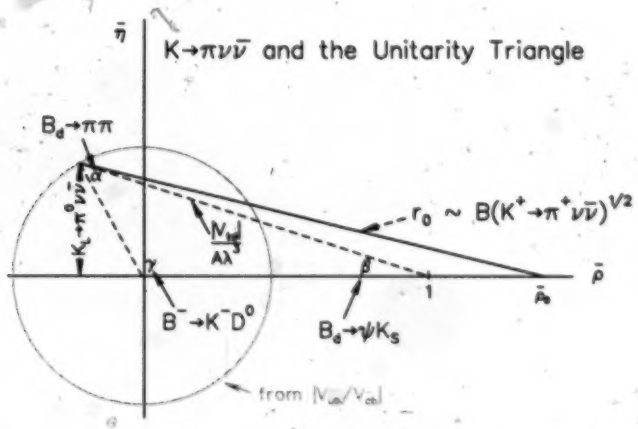

Figure 1.1: CKM triangle determination from the K and B systems.

In the Standard Model, the quark mass eigenstates are related to the weak eigenstates in the form of Cabibbo-Kobayashi-Maskawa (CKM) matrix [2]:

$$V_{CKM} = \begin{pmatrix} V_{ud} & V_{us} & V_{ub} \\ V_{cd} & V_{ts} & V_{cb} \\ V_{td} & V_{ts} & V_{tb} \end{pmatrix} \tag{1.1}$$

Using the Wolfenstein parametrization [3], V_{CKM} can be re-expressed as:

$$V_{CKM} = \begin{pmatrix} 1 - \frac{\lambda^2}{2} & \lambda & A\lambda^3(\rho - i\eta) \\ -\lambda & 1 - \frac{\lambda^2}{2} & A\lambda^2 \\ A\lambda^3(1 - \rho - i\eta) & -A\lambda^2 & 1 \end{pmatrix} \tag{1.2}$$

Hence, the task of measuring the parameters of V_{CKM} can be accomplished by measuring λ, A, ρ, and η. λ has been determined via K_{e3} decays and found to be $|V_{us}| = \lambda = 0.2205 \pm 0.0018$ [4]. $|V_{cb}|$ can be measured via B meson decays and determines A: $A\lambda^2 = |V_{cb}| = 0.040 \pm 0.003$ [8].

One could exploit the unitarity of V_{CKM} to express the matrix elements geometrically as a triangle in the complex plane (see Fig. 1.1). The axes $(\overline{\rho}, \overline{\eta})$ are defined as [5]:

$$\overline{\rho} = \rho\left(1 - \frac{\lambda^2}{2}\right), \qquad \overline{\eta} = \eta\left(1 - \frac{\lambda^2}{2}\right). \tag{1.3}$$

The branching ratio for $K^+ \to \pi^+\nu\overline{\nu}$ can be expressed as [11]:

$$BR(K^+ \to \pi^+\nu\overline{\nu}) = 4.11 \times 10^{-11} A^4 X^2(x_t) \frac{1}{\sigma}\left[(\sigma\overline{\eta})^2 + (\rho_0 - \overline{\rho})^2\right], \tag{1.4}$$

where

$$\sigma = \left(\frac{1}{1 - \frac{\lambda^2}{2}}\right)^2 \simeq 1.05, \tag{1.5}$$

$$X(x_t) = \frac{x_t}{8}\left(\frac{x_t + 2}{x_t - 1} + \frac{3x_t - 6}{(x_t - 1)^2}\ln x_t\right), \quad x_t = \frac{m_t^2}{m_W^2}. \tag{1.6}$$

A and λ are CKM parameters. Equation 1.4 determines an ellipse in the $(\overline{\rho}, \overline{\eta})$ plane centered at $(\rho_0, 0)$. A measurement of $\mathrm{B}(K^+ \to \pi^+\nu\overline{\nu})$ along with that for the neutral analog $\mathrm{B}(K_L^0 \to \pi^0\nu\overline{\nu})$ completely determines the CKM unitary triangle. Measurements of these decays are the theoretical cleanest ways of determining the CKM parameters $\overline{\rho}$ and $\overline{\eta}$. In order to confront the SM explanation of CP violation, determination of these parameters from the K system is essential. Such measurements are complementary of those obtained from the B system and any discrepancy in the values found would be a strong indicator of new physics.

1.2 CEX Background

The signature for $\pi^+\nu\overline{\nu}$ is a K^+ decay to a π^+ of momentum $P < 227$ MeV/c with no other observable product. Major background sources include the copious two-body decays $K^+ \to \mu^+\nu$ ($K_{\mu 2}$) with a 64% branching ratio and $P = 236$ MeV/c and $K^+ \to \pi^+\pi^0$ ($K_{\pi 2}$) with a 21% branching ratio and $P = 205$ MeV/c. The only other important background sources are scattering of pions in the beam and K^+ charge exchange scattering in the target.

The target for E787 is polystyrene, which contains carbon and hydrogen atoms. When the K^+ enters the target, there is a finite probability that the K^+ will undergo

Decay Modes	Branching Ratio	P (MeV/c)
$K_S^0 \to \pi^+\pi^-$	0.686	206
$K_S^0 \to \pi^0\pi^0$	0.314	209
$K_L^0 \to 3\pi^0$	0.212	139
$K_L^0 \to \pi^+\pi^-\pi^0$	0.126	133
$K_L^0 \to \pi^\pm\mu^\mp\nu$ ($K_{\mu 3}^0$)	0.272	216
$K_L^0 \to \pi^\pm e^\mp\nu$ (K_{e3}^0)	0.388	229

Table 1.1: Main Decay Modes of K_S^0 and K_L^0.

charge exchange reaction with the carbon nuclei in the target to produce a neutral kaon. The reaction can be represented by a general form

$$K^+ + {}^{12}\mathrm{C} \to K^0 + \mathcal{N} \tag{1.7}$$

where $\mathcal{N}$ represents some final state products of the ^{12}C nucleus. From the viewpoint of $\pi^+\nu\bar{\nu}$ search, the K^0 plays a crucial role as a possible background; hence a discussion on the nature of $\mathcal{N}$ and its effect on this work will be postponed until Section 4.2.2.

Due to charge conservation, hydrogen nuclei (or protons) do not contribute to this process. The charge exchange process in carbon is endothermic and has a threshold of $Q \simeq -20$ MeV. Two specific reactions from the CEX scattering are

$$K^+ + {}^{12}\mathrm{C} \to K^0 + p + {}^{11}C, \quad Q = -22 \text{ MeV} \tag{1.8}$$

and

$$K^+ + {}^{12}\mathrm{C} \to K^0 + {}^{12}N, \quad Q = -16 \text{ MeV} \tag{1.9}$$

The neutral kaon, K^0, is a linear combination of 50-50% K_S^0 and K_L^0. The decay modes for the K_S^0 and K_L^0 are shown in Table 1.1. The prompt decay of K_S^0 ($\tau = 0.089$ ns) can be rejected easily by the experimental trigger's timing gate which selects only events delayed by 2 ns. However, the longer lifetime of the K_L^0 ($\tau = 51.7$ ns) falls within the timing gate of the $\pi^+\nu\bar{\nu}$ trigger. Vetoing of decay modes involving π^0's is achieved using the photon veto system. The semileptonic decays of K_L^0 ($K_{\mu 3}^0$ and K_{e3}^0) pose a much more serious background problem. The background arises when CEX occurs and the K_L^0 decays semileptonically inside the target and the electron or muon from the decay is not detected, *i.e.*,

$K^+ \to K_L^0 \to \pi^+(l\nu)$, with $(l\nu)$ undetected.

The background is naturally highly suppressed since the relativistic K_L^0 with decay length, $c\tau = 16$ m, will usually travel out of the detector and miss the target fiducial region completely. If the K_L^0 do decay in flight, the outgoing pions will fall into the $\pi^+\nu\bar{\nu}$ signal region of 209-238 MeV/c. With the outgoing pion in the signal region, failure to detect the charged lepton will lead to a false $\pi^+\nu\bar{\nu}$ signal.

Unlike other backgrounds in the $\pi^+\nu\bar{\nu}$ analysis, the CEX background is estimated from Monte Carlo simulation. The greatest uncertainty in the simulation is the lack of (K^+,C) cross-section information at the low energy region. Most CEX data consists of bubble chamber K^+ scattering experiments in deuterium, and a few data points on K^+ charge exchange on heavy nuclei, all with extremely low statistics and more than a decade old. Typical cross-sections obtained by extrapolation from higher energies data is of the order of a few millibarn. In an effort to understand the CEX background, a special trigger was installed to capture the $\pi^+\pi^-$ decay of K_S^0 during the 1997 run. Information from the CEX special run has been used to estimate the CEX background in the $\pi^+\nu\bar{\nu}$ signal region. It is the purpose of this thesis to further untangle the CEX background by extracting the cross-section from the K_S^0 decay data.

Chapter 2

Theory

In this chapter, we will discuss the general properties of kaon-nucleon (K^+N) and kaon-nucleus interaction. The theoretical framework for the charge exchange cross-section calculation will be developed using the optical model.

2.1 Kaon-Nucleon Interaction

The interaction of $K^{\pm}$ mesons with nucleon at low energies can be understood by looking at their quark composition. K^- is made up of $\overline{u}s$, while the nucleon, say the proton contains two u's and one d. The $\overline{u}$ in the K^- and the u in the proton can annnihilate, going off, for example, as a pion leaving behind usd, a Λ or Σ^0. With the K^+ which is a $u\overline{s}$ system, no such annihilation can occur are we are left with a five-quark system $uuud\overline{s}$. The nearest inelastic channel is that of $uuu = \Delta^{++}$, $d\overline{s} = K^0$ (ΔK system) with a threshold of 1725.67 MeV.

Therefore, the K^-N interaction is strongly attractive, with many low-energy bound states and resonances. This attractive nature of K^-N greatly complicates the theoretical analysis of K^--nucleus data. On the other hand, K^+N interaction is rather weak and repulsive, exhibiting no low energy bound states or resonances. The K^+-p system has strangeness $s = +1$, baryon number $B = 1$, whereas all hyperons with $B = 1$ (Conservation of baryon number) have $s = -1$, so that there are no inelastic channels possible until the initial energy is sufficiently high for pion production:

$$\begin{aligned} K^+ + p &\rightarrow K^+ + n + \pi^+ \\ &\rightarrow K^0 + p + \pi^+ \end{aligned} \tag{2.1}$$

Due to strangeness conservation, the only inelastic channel at low energies is the charge exchange channel $K^+ + n \rightarrow K^0 + p$ [13].

Shown in Fig. 2.1 [13] is the observed K^+p total cross section data σ_T in the low energy region. The cross section is essentially energy independent and elastic up to $p_{lab} \approx$ 700-800 MeV/c. Above 800 MeV/c, the inelastic cross section rises rapidly due to pion production. The solid curves in Fig. 2.1 correspond to Martin's phase shift analysis [15]. The $s-$wave contribution (lower solid curve) totally dominates σ_T up to 350 MeV/c; while the $s-$ and $p-$waves together fit the data up to 700 MeV/c. This implies that an optical potential constructed from $l = 0$ and 1 amplitudes should provide a good description of K^+-nucleus scattering from $P_{lab} \approx$ 0-700 MeV/c. Typical cross section in this region averages around 10 mb, corresponding to a mean

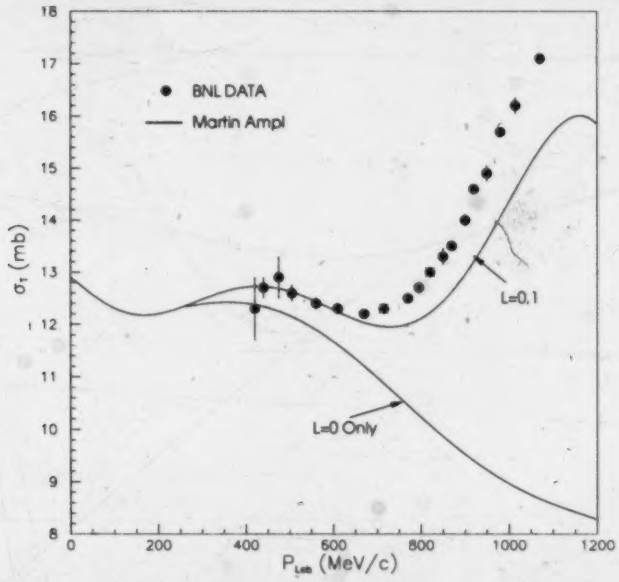

Figure 2.1: The K^+p total cross section data. Experiment values are from [14]. Shown also is the calculated $s-$ and $p-$wave contributions based on Martin amplitudes [15].

free path λ for propagation of K^+ in the nuclear medium [13]:

$$\lambda \approx \frac{1}{\rho\sigma} \approx 7\,\text{fm} \tag{2.2}$$

using a nuclear matter density of $\rho \approx 0.16$ fm^{-3}. Therefore the low momentum K^+ is capable of probing a large part of the nuclear volume, in contrast to the strongly

interacting particles ($\pi^{\pm}$) which get absorbed at the surface [12]. The small K^+N elementary cross section implies that there is little ambiguity in the reaction mechanism for K^+ induced processes. The K^+ wave function experiences little distortion upon entering the nucleus. Hence methods like plane-wave impulse approximation (PWIA) and distorted wave Born approximation (DWBA) should be quantitatively accurate for K^+ reactions [13]. These simple features makes the K^+ an attractive projectile for nuclear structure studies, since many of the ambiguities inherent in the analysis of reactions induced by strongly absorbed probes are absent.

2.2 Kaon-Nucleus Interaction

For reasons mentioned above, K^+ has been used extensively to study various aspects of the strong interaction and nuclear structure. To study possible changes of the nucleon structure in the nucleus, one would measure the ratio

$$R_T = \frac{\sigma_{tot}(\mathrm{K}^+ - \mathrm{nucleus})/A}{\sigma_{tot}(\mathrm{K}^+ - \mathrm{deuteron})/2} \tag{2.3}$$

This ratio represents a convenient isospin-averaged free nucleon target [16]. Measurements [16, 17] shows that the experimental ratios R_T lie considerably ($\approx$ 10 %) above the prediction of "conventional medium corrections" calculation performed by Siegel [18]. The conventional medium corrections were performed for K^+-nucleus interaction for carbon using a microscopic optical model which incorporates nucleon binding, recoil, and Pauli blocking corrections. According to Siegel *et al.*, the 10 % difference between observation and the optical model calculation can be attributed to the "swelling" of nucleons in the nucleus. The swelling of the nucleons effectively increases the K^+N phase shifts since the size of the K^+N interaction inside the nucleus will differ from the free one [18]. Other microscopic multiple scattering models [21, 22, 23] have been formulated to explain this discrepancy. These models, all with different fundamental postulation about the nuclear medium, improve agreement with available data over the conventional calculation. Fig. 2.2 [17] shows the experimental values plotted against the different calculations performed. While these models are different in details, they all yield a similar result, namely a density dependent cross section ratio. No experimental data has ruled out any of these phenomenological models.

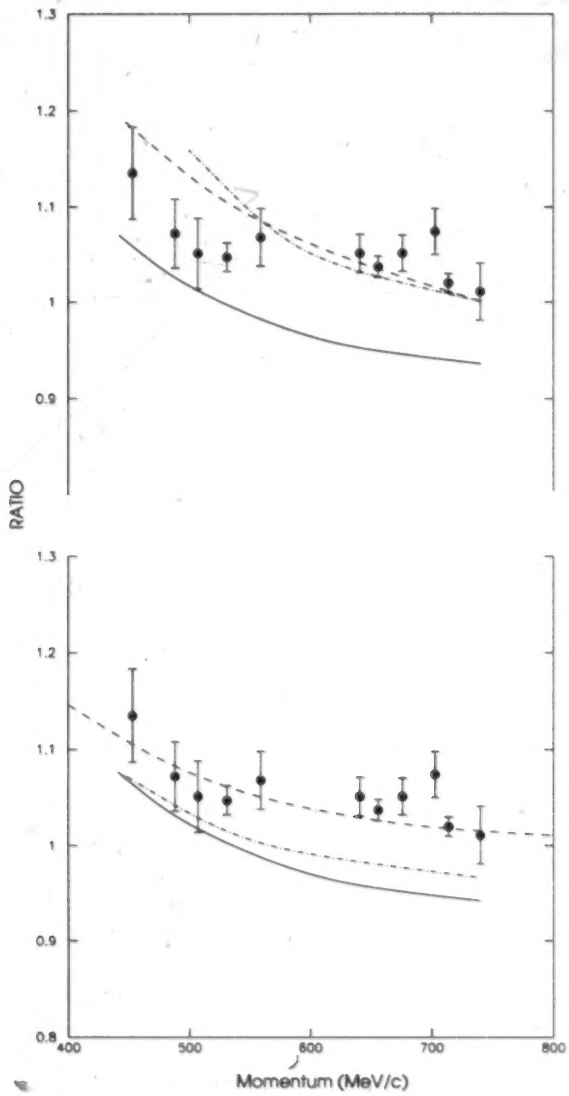

Figure 2.2: The calculated ratios R_T by Siegel [18] (solid line) and data from Krauss [17] are shown in the upper and lower figures. The 10% swelling calculation by Siegel(dashed line) and the density meson mass dependence calculation by Brown [21] (dot-dashed line) are shown in the upper figure. The lower figure includes the calculations done by Migdal [22] (dashed line) and Akulinichev [23] (dot-dashed line) that take into account the pionic degree of freedom in the nuclei.

2.3 Optical Model

The interaction K^+ with nuclei is described by the Klein-Gordon equation [13]

$$\left[\nabla^2 + k^2 - (2\epsilon_{c.m.}^{(A)} V - V_c^2)\right] \psi = 0 \quad (\hbar = c = 1) \tag{2.4}$$

where k and $\epsilon_{c.m.}^{(A)}$ are the wave number and reduced energy respectively in the center of mass ($c.m.$) system, $(\epsilon_{c.m.}^{(A)})^{-1} = E_p^{-1} + E_t^{-1}$ in terms of the $c.m.$ energies for the projectile and target particles, respectively. V_c is the Coulomb potential due to the charge distribution of the nucleus, and $V = V_c + V_{opt}$. Using the simplest possible "$t\rho$" approximation [24] form for the optical potential,

$$2\epsilon_{c.m.}^{(A)} V_{opt}(r) = -4\pi F_k b_0 \rho(r) \tag{2.5}$$

where F_k is a kinematical factor resulting from the transformation of amplitudes between the KN and K^+-nucleus $c.m.$ systems and b_0 is the value of the KN scattering amplitude in the forward direction. The factor F_k takes the form

$$F_k = \frac{M_A \sqrt{s}}{M(E_t + E_p)} \tag{2.6}$$

M is the free nucleon mass, M_A is the mass of the target nucleus and $\sqrt{s}$ is the total projectile-nucleon energy in their $c.m.$ system. The nuclear density distribution $\rho(r)$ is normalized to A, the number of nucleons in the target nucleus. The carbon nuclear density takes the form of a modified harmonic oscillator density distribution [25]

$$\rho(r) = (\alpha + \beta r^2) \exp^{-\gamma r^2}, \quad \alpha = \frac{4}{R^3 \pi^{1.5}}, \quad \beta = \frac{2(A-4)}{3\pi^{1.5} R^5}, \quad \gamma = \frac{1}{R^2}, \tag{2.7}$$

where $R^2 = 2.5$ fm^2. The K^+N amplitude b_0 was taken from K^+N phase shifts as given by the SAID program [26]. The computation was performed by Friedman to obtain the total reaction cross section. The total CEX cross section is then estimated by [27]

$$\sigma_{cex} = \frac{[\sigma_t - \sigma e]_{KN}}{[\sigma_t]_{KN} + [\sigma_t]_{KP}} \times \sigma_R \tag{2.8}$$

where σ_R is the reaction cross section for carbon, σ_t is the total cross section, and σ_e is the total elastic cross section with KN, KP representing K^+-neutron and K^+-proton scattering respectively. Those cross sections are given by the SAID program as well. A plot of the total CEX cross section is shown in Fig. 2.3. The reaction cross section,

σ_R, of carbon contains the inelastic and CEX components. The numerator term in the ratio is a purely inelastic part in K^+-neutron scattering, which translate to CEX scattering. The denominator in the ratio accounts for the overall K^+-neutron and K^+-proton contribution in K^+-nucleus scattering. Hence, the ratio serves to extract the CEX component from the reaction cross section. It should be noted that this estimation is only valid within 10%.

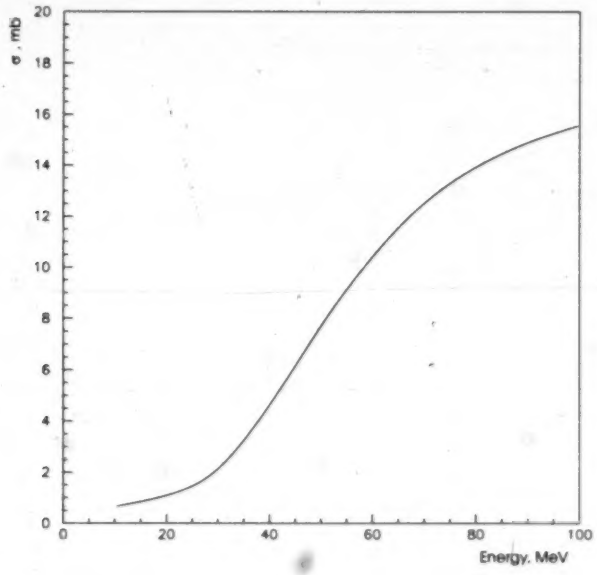

Figure 2.3: Total CEX cross section based on optical model calculation.

Chapter 3

The E787 Detector

3.1 Detector Description

The detector consists of the following subsystems : beam instrumentation, an active fiber target where the kaon come to rest, a central drift chamber, a range stack of plastic scintillator, and a system of photon vetos. A picture of the top half of the cylindrical detector is shown in Fig. 3.1.

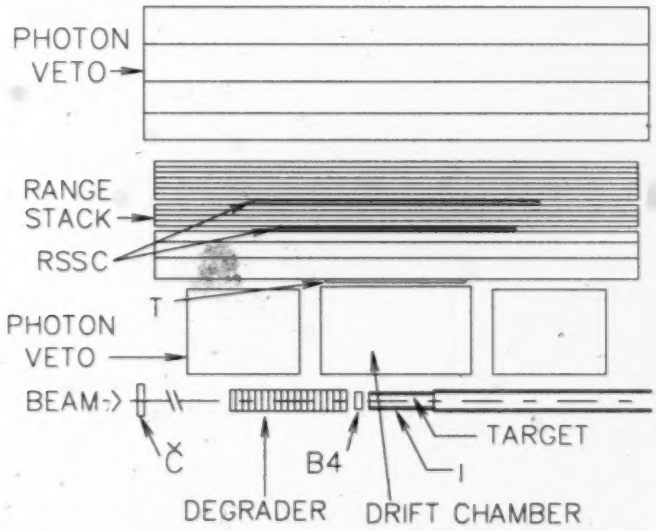

Figure 3.1: Schematic for the E787 detector.

3.1.1 Beam

E787 is situated in the Low Energy Separated Beam III (LESB III) at the Alternating Gradient Synchrotron (AGS) at BNL. Towards the end of 1997 run, 670 MeV/c kaons[1] were delivered in 1.6 second spills, one every 3.6 seconds. Each spill contained roughly 4×10^6 K^+'s and 1×10^6 π^+'s. About 1.2×10^6 K^+'s made it to the stopping target per spill.

The kaon beam first passes through a Čerenkov counter. Čerenkov radiation made by relativistic particles passing through transparent media is exploited to tag kaons and pions using a lucite radiator. The Čerenkov light is directed into 14 K^+ phototubes (C_k) or directed into 14 π^+ phototubes (C_π), depending on the velocity of the particles. The emerging kaon beam will encounter two beam wire proportional chambers (BWPC's), separated from each other by about 90cm. The BWPC can identify multiple beam particles close to each other in space and time. After the BWPC, the beam enters the degrader, where it will be slowed down through ionization energy loss so that the beam particles can be stopped in the target. The first 37.5 cm of the degrader is made of beryllium oxide, while last 10 cm is made of lead oxide doped glass. The latter active degrader (or the lead glass counter) is instrumented with phototubes and is used to detect Čerenkov light from the beam pions or photons coming from kaon decays in the target. Sandwiched between the lead-glass counter and the target is the B4 hodoscope which consists of 2 planes of 8 scintillating fingers each. This counter is used to detect beam particles that make it through the degrader.

3.1.2 Target

After passing through the B4 hodoscope, the kaon beam enters the target where it stops and decays at rest. The target is made of 413 5-mm square plastic scintillator fibers, each 310 cm in length and connected to a phototube. The target signals are fed to ADC's, TDC's and 500 MHz CCD transient digitizers. For $\pi^+\nu\bar{\nu}$, the kaons will be slowed down in the target and typically come to rest roughly in the center of the detector. However, kaon CEX can occur in flight during the K^+ passage through the target.

In general, the incoming K^+ will hit only a few target fibers, depositing > 5 MeV in each. The outgoing pions from the decays will travel perpendicular to the fibers,

[1]Before run number 34900, the momentum was 710 MeV/c

depositing $\approx$ 2 MeV in each. The time and energy information help to distinguish the kaon fibers from the pion fibers.

Surrounding the target, parallel to each hextant edge, are 6 scintillating counters called the Inner Counters (I-counter). The six I-counters are 24.1 cm in length and define the fiducial region in z of the target. Another set of six scintillators overlaps the downstream end of the I-counters. This set has been designed for vetoing the hits outside the fiducial region (hence the name V-counters).

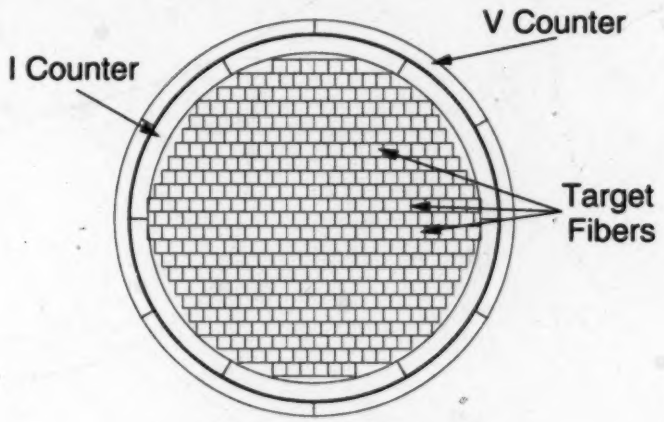

Figure 3.2: Endview of the target.

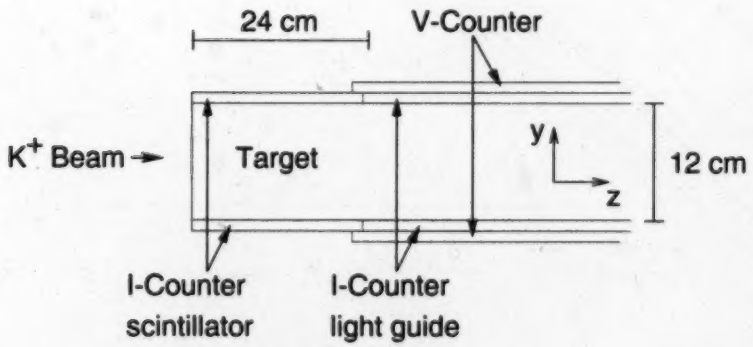

Figure 3.3: Sideview of the target.

3.1.3 Drift Chamber

Surrounding the target subsystem is the drift chamber, also known as Ultra Thin Chamber (UTC). Charged particles leaving the target are bent by the 1 Tesla magnetic field. The UTC records the charged track of these particles, allowing their momenta to be measured. The UTC has 12 layers of drift cells (each with an anode wire) arranged in 3 superlayers and filled with an Argon/Ethane/Ethanol gas mixture. The 3 superlayers are separated by passive buffer regions containing nitrogen. Six foils are etched with helical cathode stripes. These strips provide z measurements that can be used to determine the dip-angle, the angle of the charged track with respect to the plane normal to the beam. The ionization drift velocity in the UTC is about 40 μm/ns.

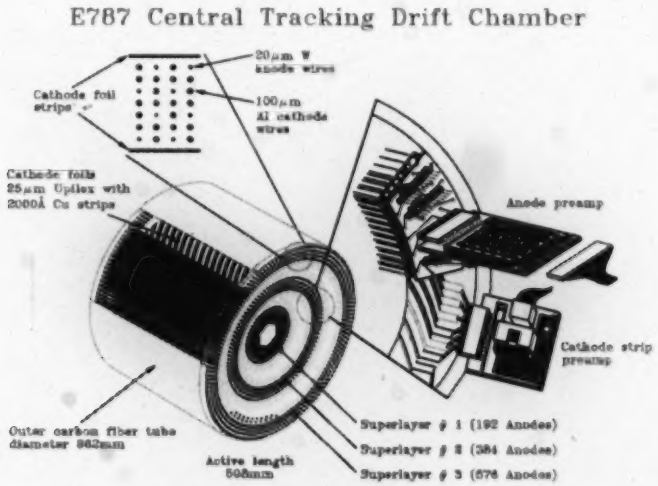
E787 Central Tracking Drift Chamber
20μm W anode wires
Cathode foil strips
100μm Al cathode wires
Cathode foils 25μm Upilex with 2000Å Cu strips
Anode preamp
Cathode strip preamp
Outer carbon fiber tube diameter 862mm
Active length 508mm
Superlayer # 1 (192 Anodes)
Superlayer # 2 (384 Anodes)
Superlayer # 3 (576 Anodes)

Figure 3.4: E787 Drift Chamber

3.1.4 Range Stack

Surrounding the UTC is the range stack. The range stack acts as a calorimeter recording the energy of the particles which enter it. It also measures the range of the particle's path as it travels through the range stack. The range stack is made up of 20 layers of 1.905 cm thick $\times$ 182 cm long scintillating counters and 1 layer of 0.635 cm $\times$ 52 cm long scintillating counter, arranged in 24 sectors. The first layer, also

the T counter, defines the solid angle acceptance of the detector. Each range stack is instrumented with a phototube at each end. The pulses from these phototubes are delivered to ADC's and 500 MHz transient digitizers (TD's), and they are also discriminated for use in the trigger. The TD's are especially useful for observing the $\pi^+ \rightarrow \mu^+ \rightarrow e^+$ decay sequence in the range stack in which the π^+ comes to rest (called the stopping counter).

Another component of the range stack are the straw-tube tracking chambers (RSSC). They are embedded in layer 10 and 14 of the range stack. These chambers provide refined measurements of ϕ and z.

3.1.5 Photon Veto

Surrounding the range stack is the barrel veto (BV) which is a photon detection system. It is made up of lead scintillator sandwich counters of alternating 1mm thick lead slabs and 5.4 mm thick scintillators. The BV is designed to detect photons of a few MeV up to around 250 MeV. The BV is about 15 radiation length thick, and the fraction of energy deposited in the scintillator is 0.3. The scintillators are coupled with phototubes at both end, and instrumented with ADCs and TDCs.

The areas up and down stream of the UTC are filled with the endcap (EC) veto system. The endcaps are made of pure CsI crystals useful for detecting photons with large dip angle. The crystals are coupled to the phototubes instrumented with 500 MHz CCD transient digitizers.

3.2 CEX Signal in the E787 Detector

From the discussion of the CEX background in Section 1.2, the easiest way to study CEX for E787 is to detect the charged 2π decay of K^0_S from the K^+ charge exchanging with the target. As a result of the K^0_S's short lifetime, the daughter pions would have an almost prompt timing. Moreover, the two oppositely charged tracks signature can be detected easily enough. These two prominent features of the decay mode are implemented in the trigger to facilitate the K^0_S detection.

The cross section of the CEX process influences where the interaction takes place within the target. Higher energy K^+'s charge exchange close to the target face since the cross section is higher. Lower energy K^+'s are derived either from initial low energy K^+ entering the target or higher energy kaon lossing energy through ionization

in the target. Constraints from the slightly smaller cross section and path length to achieve low energy mean that the interaction point will shift downstream in the target. What can be detected in this experiment is the K_S^0 decay vertex (from track fitting routines) and again the short lifetime of K_S^0 means that the decay vertex position is very close to the real CEX interaction position.

The two-body decay of K_S^0 would also give nice kinematic peaks for the outgoing pions. For low energy kaon, the angle between the outgoing pions would simply be 180° or back-to-back tracks. A near isotropic angular distribution is also expected from this low energy interaction.

3.3 The CEX Trigger

The trigger determines which events will be written to tape. Fast decisions must be made as the events are coming in. The CEX trigger only uses rather crude selection criteria to reject background events. There is only one level of trigger requirement for the CEX. The Level 0 trigger installed for CEX is defined as follows:

- KBeam : KBeam is a fourfold coincidence, requiring hits in at least 9 of the 14 Čerenkov counter kaon phototubes, a hit in the B4 counter, energy in the target, and a signal derived from the AGS spill structure that determines the useful part of the beam spill. KBeam = $C_k \cdot$ B4 $\cdot$ TTsum $\cdot$ spill. Kbeam defines the entry of a kaon into the target.

- $\overline{\text{DELCO}}$: Signal from the IC is put into delayed coincidence with the KB using a delayed time of 2.0 ns. The time differences between the IC and the KB will give the kaon lifetime. Essentially the DELCO requires the kaon to stop and decay in the target. By inverting the delayed coincidence, the prompt decay of the K_S^0 will be triggered.

- 2(T·2) : The basic T·2 requires a coincidence between the first two layers in the same sector of the range stack. The path of the particle that satisfied this trigger requirement is referred to as charged track. In this case, only two charged track events will be triggered. The T·2 aslo requires a coincidence with the IC in order to improve the $\pi^+\nu\overline{\nu}$ acceptance.

- $6_{ct} + 7_{ct}$: Either range stack layer 6 or layer 7 must be struck by the charged track associated with the T·2 hit.This eliminates events with very short tracks.

This requirement will be satisfied if either one of the charged tracks associated with a T·2 reaches the RS layer 6.

- $\overline{19_{ct} + 20_{ct} + 21_{ct}}$: The track is not allowed to enter range stack layers 19-21. This vetoes $K_{\mu 2}$'s, which have longer range. It is basically the online μ veto.
- $\overline{\mathrm{BV} + \mathrm{EC}}$: Events with energy in the barrel or endcap photon detectors are vetoed if this energy is in coincidence with the charged track. The barrel veto threshold is set at about 15 MeV photon while the endcap is about 20 MeV.
- $\overline{\pi_B}$: Similar definition as KBeam except it requires hits in the pion Čerenkov phototubes. Serves to veto out any pion entering the target during spill.

The last two triggers are used to veto out K^+ decay in flight and Dalitz decay. The triggers described above constitute the Level 0 trigger. The $K^+ \to \pi^+ \nu\overline{\nu}$ trigger has a second layer of trigger called Level 1.1 that provides discrimination for π and μ decay in the range stack.

3.4 CEX Data

Near the end of 1997 run, the CEX trigger was installed. The information from each subsystem was digitized and recorded to 8 mm tape for each event passing the trigger. A total of nine tapes of CEX data were collected, along with a monitor data tape, giving a total of K_{BLive}[2] of 16.51×10^8.

[2] K_{BLive} is the number of kaons that entered the detector during the run.

Chapter 4

Offline Analysis

Basic offline event handling and reconstruction was done with the E787 software KOFIA version 2.1 and Monte Carlo event simulation by UMC version 6 beta release. KOFIA is used extensively for reading the data tapes, unpacking the raw detector information, and filling the FORTRAN common blocks into user-friendly HBOOK ntuples. The Monte Carlo program, UMC, is used to simulate the online trigger performance of the detector.

Once the ntuple files were generated by KOFIA, further studies can be performed on the CEX data. The analysis strategy adopted in this work is as follows:

- Background studies. We need to understand the background contained within the sample so that cuts can be developed to remove these contaminations.
- Event Selection. Application of cuts developed based on the background studies. The resulting sample will consist of CEX events.
- Acceptance Measurement. The efficiencies of the detector and cuts are measured.
- Normalization. The kaon flux entering the target is measured here and will be used as a normalization factor in calculating the cross section.
- Cross section calculation.

4.1 Event Reconstruction

The data collected undergo a basic reconstruction using KOFIA routines. The events are reconstructed under the assumption that they are $K_S^0 \to \pi^+\pi^-$ resulting from the

kaon-nucleus charge exchange interaction within the target. Reconstruction begins in the range stack where the rates are lowest. After finding a track in the range stack, the code searches for a matching UTC track. The UTC track is extended into the target to search for possible pion track. Kaon fibers in the target also appear along UTC track extrapolation. Kaon time, energy information from these fibers can then be used to identify various kaon hits in the beamline detectors. Below is the detailed description of the steps involved in the reconstruction.

The routine **RD_TRK** is called to perform a charged track recognition in the range stack. **RD_TRK** attempts to identify the sector that produced the T·2 signal by looking for layer T and layer 2 counters with hits close to the detector strobe time (the time of the charged track as recorded by the trigger). After finding the T·2 sector, **RD_TRK** works outward through the range stack, looking for counters with hits at track time until the end of the track is reached. Once the list of RS counters for the charged track is known, **TRKTIM_RD** will compute a single time for the track (called **TRS**) by averaging together the times of the hits in the various counters.

Next the UTC reconstruction code, **UTC_TRACK**, will search for tracks in the sector where **RD_TRK** flagged as the RS track entry point. **UTC_TRACK** fits a circular track to the isochrones of struck UTC wires, and then information from the cathode strips is used to perform a straight line fit to the $\alpha - z$ plane. A helical track is then formed giving information on the track momentum plus the position and direction of the track when exiting the target and when entering the range stack. If more than one track points to the same T·2 sector, the track that comes closest to the first sector crossing in the RS is chosen.

Once the UTC track fitting is done, **RD_TRK_ANAL** performs a careful accounting of the energy deposited and the range of the charged track in the range stack. The energy is determined by summing up the ADC energies of the RS counters. In the RS energy measurement, corrections are applied for dead material in the RS and outer wall of the UTC. Saturation of the energy-light relation in the RS scintillator is also corrected. All the corrections require an assumption about the identity of the particle. We assume the particle to be pions for these corrections. Then another correction is needed for the $\pi \rightarrow \mu$ decay. The energy for a π^+ track as measured by the RS usually includes the $\pi \rightarrow \mu$ decay. It is therefore necessary to subtract the 4.12 MeV kinetic energy from the measured RS energy in a π^+-track.

After the RS energy is determined, the routine will proceed to measure the track range. The track range is measured using a track fitter. The fitter is given the RS

entry point as measured by the UTC. The fitter then attempts to find the best track matching between the UTC track and the RS track through minimization based on the sector crossings, RSSC hits, and energy in the stopping layer. The best-fit track is then traced through a detailed geometrical description of the RS to determine the range up to the stopping layer. The stopping layer energy is used to estimate the stopping layer range.

After the range routines, the target analysis code, **SWATH**, is run. The UTC track is extrapolated back into the target to define a 2 cm wide swath on which to look for kaon and pion fibers. Pion fibers should all lie along the swath, and the kaon fibers should be in a cluster that touches the swath. A likelihood function uses energy, time, and distance-from-UTC-extrapolation to determine if each fibers should be labeled a pion fiber. To determine the kaon decay vertex, an updated version of **SWATH** is used. The "standard" version of **SWATH** determines the vertex by averaging two extreme-tip kaon fibers on the UTC track circle. This leads to ambiguity when the kaon enters in the direction of the UTC track in the target $x-y$ view. The new version searches the B4 counter for a hit in time with the kaon cluster in the target, and the $x-y$ location of this hit tells us where the kaon entered the target. The kaon decay vertex is defined as the center of the kaon fiber on the swath and farthest from the target entry point. This method is shown to result in better range calculation in the target.

All the routines mentioned above except **SWATH** are capable of performing multiple track fitting and searching. To get detailed target information for the second charged track, **SWATH** is re-ran with the second track index passed as an argument. The kaon fiber information between the first and second passes of **SWATH** should be identical. Each track would also have a set of pion fibers associated with it. Finally there may be a set of fibers that fail to be tagged either as kaon or pion fibers; they are classified as gamma fibers. Assignment of fibers to each track is done at the ntuple-level using **trkfiber**.

The KOFIA analysis code simply performs the RS-UTC-TG reconstruction, rejecting any events that failed the reconstruction routines, and books the physical quantities of interest into ntuple format. It is much simpler to perform event selection at the ntuple level due to the relative small size in this analysis. Performing multiple passes of data reduction and selection at the KOFIA level is inefficient.

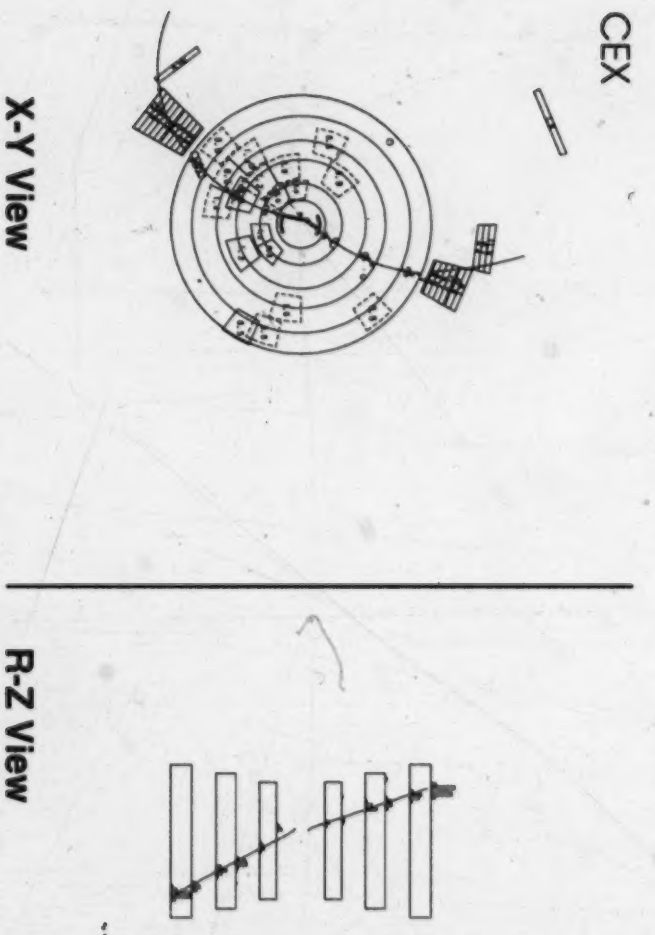

Figure 4.1: An example of a reconstructed charge exchange event.

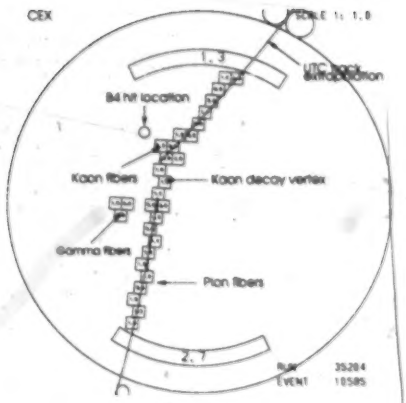

Figure 4.2: Close up view of the Target Reconstruction. Shown are the different fiber types and the energies associated with each fiber. The kaon fibers have much higher energy than the pion fibers. The B4 hit position shows the entry point of the K^+.

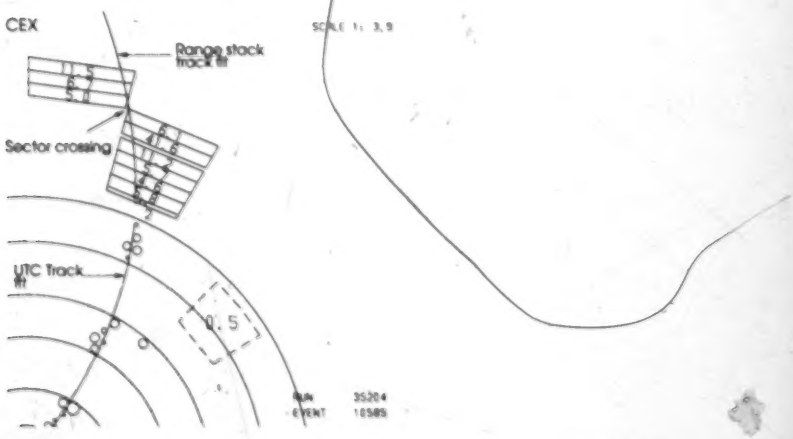

Figure 4.3: Close up view of the range stack track. The track extended from the UTC into the RS and then cross-over into a different sector.

4.2 Interaction Energy

In the usual nuclear scattering experiment, the interaction energy is defined by the energy of the beam directed toward the target. The stopped kaon used in the $\pi^+\nu\overline{\nu}$ search is obtained through the ionization energy loss of the K^+ traversing the target. Hence our energy is defined by the energy loss dE/dx of the K^+ instead.

4.2.1 B4 Energy Calibration

By selecting stopped kaon which decays as $K^+ \rightarrow \mu^+\nu$, the energy profile of the kaon entering the target can be reconstructed. The good $K_{\mu 2}$ events are selected by applying these cuts [1].

- IC Bit: Make sure that the IC has a hit.
- STLAY: Online and offline reconstructed stopping layer must agree. To remove photons or accidentals which overlap the track.
- RSHEX: Cut events with hits in the stopping hextant and layer, where the hits are not part of the track.
- TRKTIM: Cut events whose range stack track time could not be found.
- UTC/RANGE: Cut events which are not reconstructed properly in the UTC, and/or have bad matching between UTC and RS.
- Delco bit: Online delayed coincidence bit. Remove kaon decay in flight.
- TARGET: Ensure overall good target reconstruction and consistent target values for kaon.
- COS3D: Cut events with $|\theta_{\text{dip}}| < 30°$.
- DELCO: Apply offline delayed coincidence. A rather tight cut is applied to ensure that only stopped kaon is selected. Serves to remove kaon decay-in-flight. There is also a set of timing consistency cuts applied to remove beam background.

[1] These cuts are used in the standard $\pi^+\nu\overline{\nu}$ analysis. Full description of the cuts can be find in E787 Technote 326.

- **BEAM**: Removed π scattering contamination from the sample. Also cleans out any possible beam background in the sample.

The momentum, energy, and range peak of the resulting events are shown in Fig. 4.4.

The B4 hodoscope dE/dx pulse height (**B4ABM2**) provides a measurement of the energy loss of the kaon before it enters the target. This is related to the kaon energy. The **B4ABM2** distribution of the clean $K_{\mu 2}$ events are plotted in Fig. 4.5. For each value of **B4ABM2**, we bin the total energy the kaon deposited in the target (**Ek**). The **B4ABM2** is calibrated such that the minimum ionizing pion from the beamline has a value of 1. The spread in the **Ek** profile plot is around 10 MeV. Factors contributing to this 10 MeV spread are (i) scattering within the B4 hodoscope, (ii) energy straggling in the target, and (iii) multiple scattering in the target. It is a combination of resolution of the B4 and the target energy measurements.

The decay vertex position (**tgz**) is used in conjunction with the energy deposited in the target. The same binning process is done for the variable **tgz**. An expected energy value is calculated for each value of **tgz**. The weighted mean between the target energy **Ek** and decay vertex energy E(**tgz**) gives the final B4 energy calibration. The relationship is shown in Fig. 4.6, and a resolution of around 8 MeV is obtained. By simple argument of energy loss through dE/dx, one would expect a $1/\beta$ relation between **B4ABM2** and **Ek**. Deviation from the $1/\beta$ behavior is observed for **B4ABM2** $<$ 1.7 and **B4ABM2** $>$ 3.3. A low **B4ABM2** is indicative of a high energy kaon entering the target. The statistics are low in this region since the high energy kaon will come to rest much further downstream in the target, out of the geometrical acceptance of the detector. The curve seems to flatten out for **B4ABM2**$>$3.3. The low energy kaon may not deposit enough energy in the target to pass the KBeam trigger, the basic definition of kaon entering the target. The preset 25 MeV threshold on the target energy sum in the KBeam trigger restricts the K^+ passing the trigger. Coupled to this trigger bias, is the Landau fluctuation which distorts the **Ek** spectrum. The **Ek** distributions for the high, low, and intermediate kaon energy are plotted in Fig. 4.7. Based on these considerations, the "good" sample of kaons is chosen to be 1.8 $<$ **B4ABM2** $<$ 3.2.

After the completion of the B4 energy calibration, we can then determine the CEX interaction energy using

$$E_{int} = \textbf{Ek}(\text{B4}) - \textbf{Ek}(\text{observed}) \tag{4.1}$$

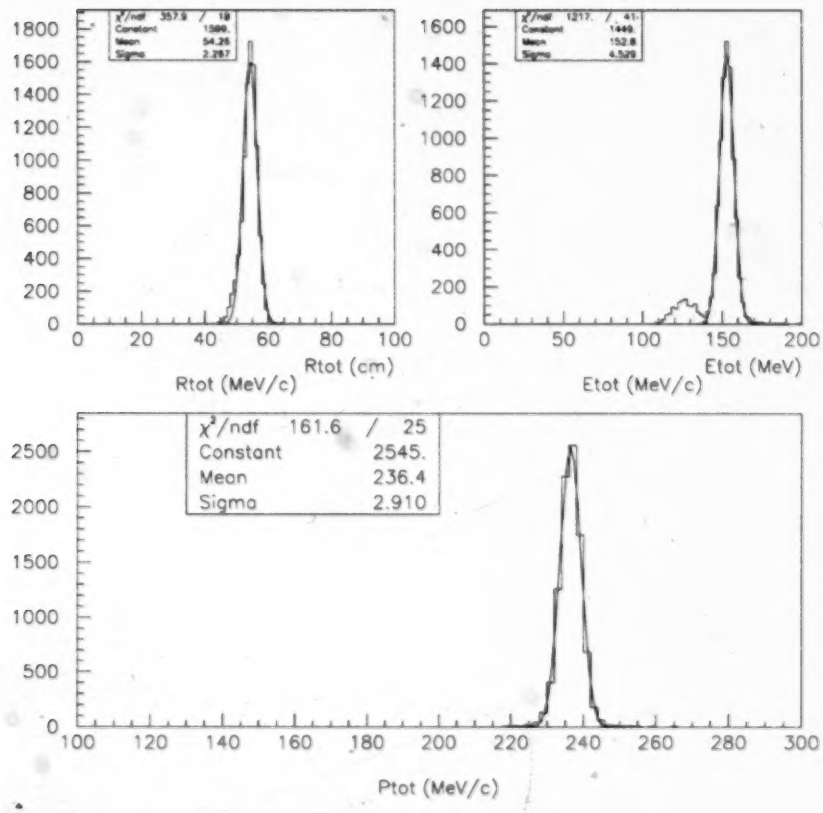

Figure 4.4: Range, energy, and, momentum distributions for $K_{\mu 2}$ after selection cuts. The low side tail in **Etot** and **Rtot** distributions is due to muon tracks that penetrate pass RS layer 21; the range and energy deposited outside the range stack is not accounted for by the reconstruction code.

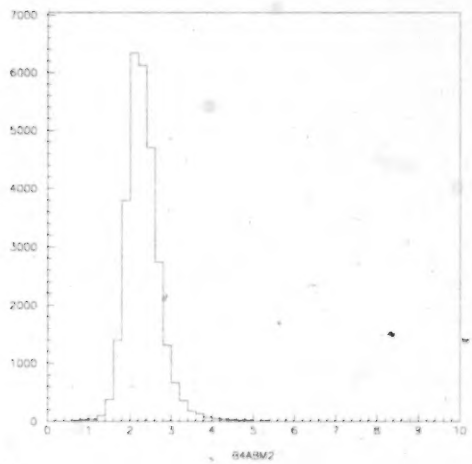

Figure 4.5: **B4ABM2** distribution for $K_{\mu 2}$ after selection cuts

with **Ek**(B4) as the energy the kaon has when entering the target and **Ek**(observed) is the energy the kaon deposited in the target. The difference of the two variables yields a missing energy which correspond to the interaction energy after corrections. The calculation has taken into account the saturation of the energy-light relation in the target fibers. The next part will discuss the systematics and limitation in determining the true interaction energy.

4.2.2 Systematic Uncertainty of Energy Measurement

Until now we have treated only the neutral kaon, and ignored all other final state products arising from the CEX interaction. As in many nuclear processes, the number of channels available for this interaction is large. At high energy, the interaction can be treated purely as a kaon-nucleon interaction since all the other nucleons are merely spectators. Typically after interacting, the proton will be dislodged from the nucleus with a certain momentum. This proton will then scatter with the surrounding atoms and loses energy. At low energies the kaon will interact with the whole nucleus; every nucleon within the nucleus will participate in the interaction. The proton resulting from the interaction may or may not be dislodged from the nucleus. If it does leave the nucleus, it would have the same fate as the high energy proton. There is a possibility

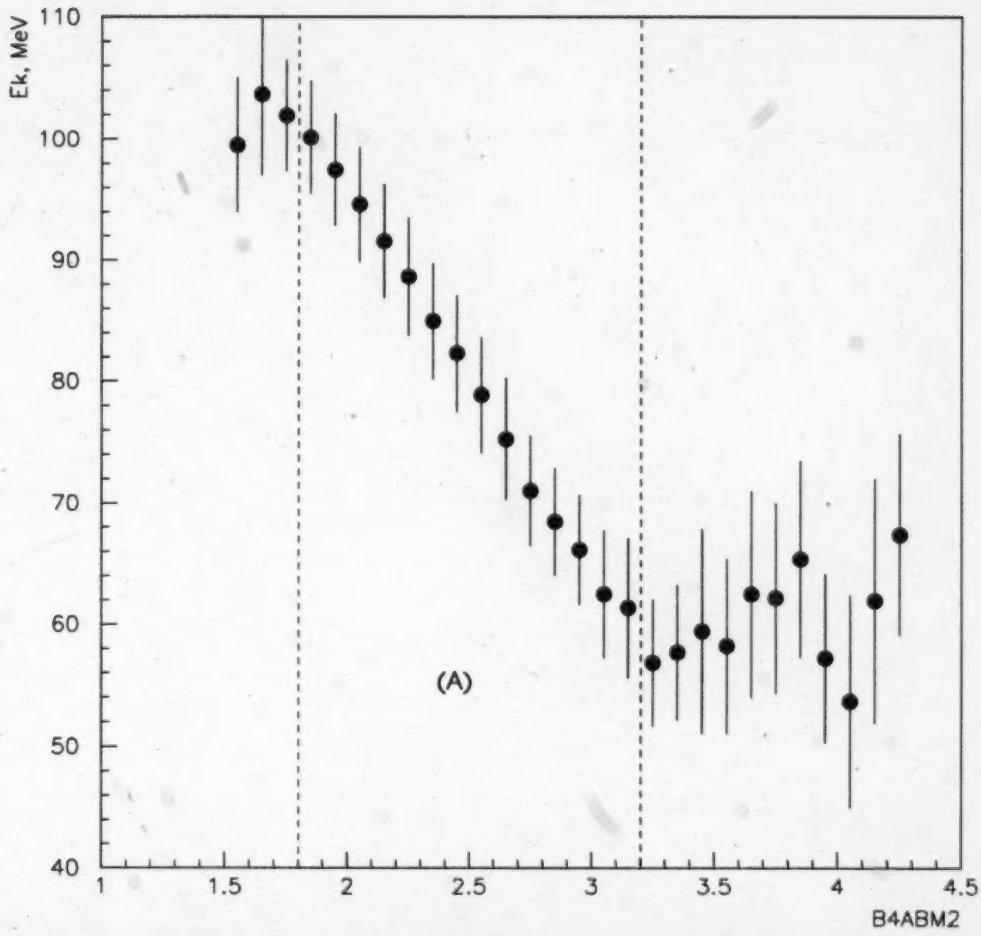

Figure 4.6: Calibration curve for **B4ABM2** and **Ek**. The error bar is a measure on the energy resolution. Region (A) is defined to be the valid of the calibration curve. Only kaons with **B4ABM2** between 1.8 and 3.2 will be selected.

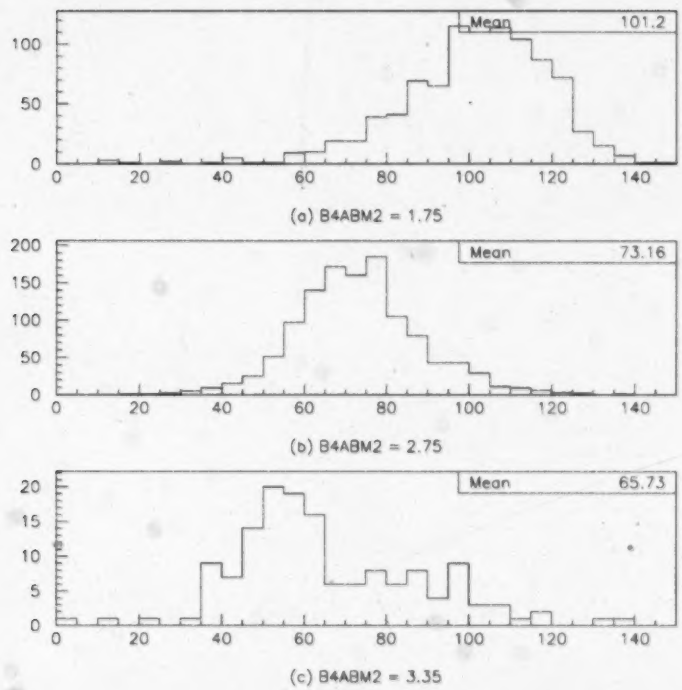

Figure 4.7: **Ek** distributions at different kaon energy regimes. The energy shift can be clearly seen. Notice the low statistics in the high and low energy region. A high energy tail can be seen in (c).

that the proton will just remain in the nucleus, or in some cases, scatter or interact with the other nucleons within the nucleus. For example, the proton could knock a neutron or proton out from the nucleus.

Based on the discussion above, it is obvious that the target energy measurement, Ek, suffers from a systematic uncertainty in that the final state products from ^{12}C cannot be de-coupled from the K^+. No absolute energy determination can be made to account for all channels. Such systematics do not exist in a transmission experiment where the energy is well determined by the beam momentum, and the final states products complication is removed by detecting only the emerging particles. This fundamental constraint will basically limit the accuracy of the results in this work. Since the fundamental CEX process involved $n \rightarrow p$, we assume two hypotheses for the reaction:

1. $K^+ + {}^{12}C \rightarrow K^0 + p + {}^{11}C^*$, $Q = -22$ MeV, with an emission of a proton, and,
2. $K^+ + {}^{12}C \rightarrow K^0 + {}^{12}N$, $Q = -16$ MeV, with no emission of proton.

Kinematically, the hypothesis (2) is more favored than (1) since the proton does not have to break loose from the nucleus. Dynamically, it is unknown if any processes would favor either reaction. Hence we will proceed by giving both hypotheses equal weighting or occurence for the CEX reaction. The differences in results from these two hypotheses will give a measure on the systematic uncertainty in our choice of equal weight for both channels. Interaction energy determination for hypothesis (2) is given by Equation 4.1. Now we will discuss the case with a proton emerging from the nucleus.

Because of its short range, the proton will contribute additional energy to the kaon fibers. It is very difficult to distinguish the proton from the kaon since there will simply be a blob of target hits classified as kaon fibers by the reconstruction software. The proton energy spectrum can be estimated from kinematics. An upper limit is given simply by using energy conservation:

$$T_p = T_{K^+} - T_{K^0} - T_{recoil} + Q \tag{4.2}$$

T_{K^0}, the K_S^0 kinetic energy is calculated using

$$T_{K^0} = \sqrt{p^2 - m^2} - m, \quad p^2 = \vec{p}_1 \cdot \vec{p}_2 \tag{4.3}$$

where m is the K^0's mass and $\vec{p}_i$ is the momentum vector for each pion track. Since measured K^+ energy $T_{K^+}^{meas}$ (= **Ek**) is a combination $T_p^{sat}+T_{K^+}^{act}$, the raw or unsaturated proton energy is first saturated and subtracted from E_{int}, giving

$$E_{int}^{real} = \textbf{Ek}(\text{B4}) - \textbf{Ek}(\text{observed}) - T_p^{sat} \tag{4.4}$$

Both unsaturated and saturated proton energy spectrum are shown in Fig. 4.8. The unsaturated proton energy spectrum represents the actual energy of the proton in the target. The saturated spectrum is the visible energy detected and is a result of the fluorescent energy-light property of the scintillator. The proton energy averages around 20 MeV before saturation. The saturation effect lowers the visible energy spectrum to around 10 MeV, with a rather significant high energy tail. At this moment, the reader may wonder why no correction is made for the nucleus recoil. The nuclear recoil energy typically is around 5 MeV due to its heavy mass. Assuming a 5 MeV recoil energy, saturation effect in the target scintillator will effectively render the recoil correction insignificant.

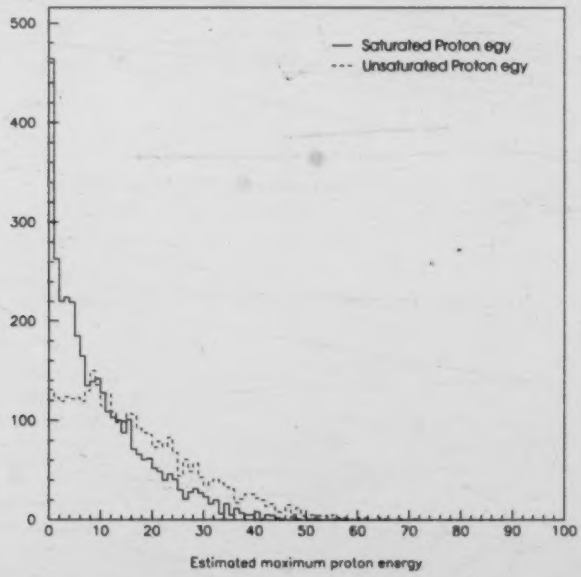

Figure 4.8: Proton energy spectrum from CEX interaction. The unsaturated or raw energy spectrum is averages around 20 MeV. However, saturation effect lowers the visible energy of the proton.

Decay Mode	Branching Ratio, %	Momentum, MeV/c
$K^+ \to \pi^+\pi^0$	21.16	205
$K^+ \to \pi^+\pi^+\pi^-$ ($K_{\pi 31}$)	5.59	125
$K^+ \to \pi^+\pi^0\pi^0$ ($K_{\pi 32}$)	1.73	133
$K^+ \to \pi^0\mu^+\nu_\mu$ ($K_{\mu 3}$)	3.18	215
$K^+ \to \pi^0 e^+\nu_e$ (K_{e3})	4.82	228

Table 4.1: A list of kaon decay modes as possible background in CEX.

4.3 Events Selection

The sample that has been successfully processed by KOFIA contained the CEX (tagged as $K_S^0 \to \pi^+\pi^-$) and a variety of background events. Certain offline cuts have to be applied to get a clean sample of the CEX events. The sections below will discuss the different cuts used in selecting the CEX events and their effectiveness in removing the background.

4.3.1 Backgrounds

A simple set of topological cuts (see Section 4.3.2) is first applied to obtain a sample for background studies. The resulting sample would contain a combination of K^+'s decay-in-flight and the $K_S^0 \to \pi^+\pi^-$ decay. Hence, Fig. 4.9 can provide some insights as to the backgrounds that would contaminate the CEX sample. The sources of background one would expect is any kaon decay modes producing 2 or more charged particles. Listed in Table 4.1 are major kaon decay modes that could contribute as backgrounds. Any decay modes with branching ratio less than 1% can be safely ignored since we are dealing with a K_S^0 decay mode with branching ratio 68%.

$K_{\pi 2}$ Decay

The single largest source of π^+ for any K^+ decay comes from the $K^+ \to \pi^+\pi^0$ decay mode which has a branching ratio of 21%. For this decay, each pion emerges with a momentum of 205 MeV/c. The π^0 decays instantly into two photons. But about 1.2% of the time, the π^0 could Dalitz decay ($\pi^0 \to \gamma e^+e^-$) or the resulting photon could pair create ($\gamma \to e^+e^-$). This mechanism results in a three charged particles decay which may satisfy the two T·2 trigger. Ideally, TRKCUT would have eliminated such an event if the UTC tracking is able to fit all three tracks. The electron will travel

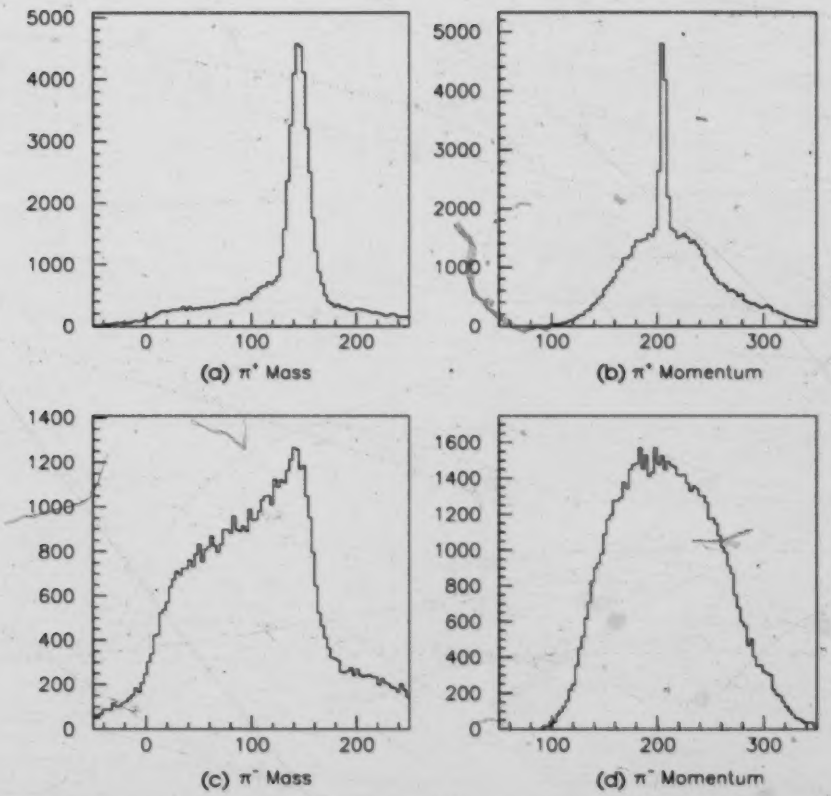

Figure 4.9: Mass and momentum spectrum for events surviving the basic topology cuts. The negative mass values are caused by detector resolutions and the pion hypothesis used in the energy corrections. Positive track is defined as π^+ while negative track π^-.

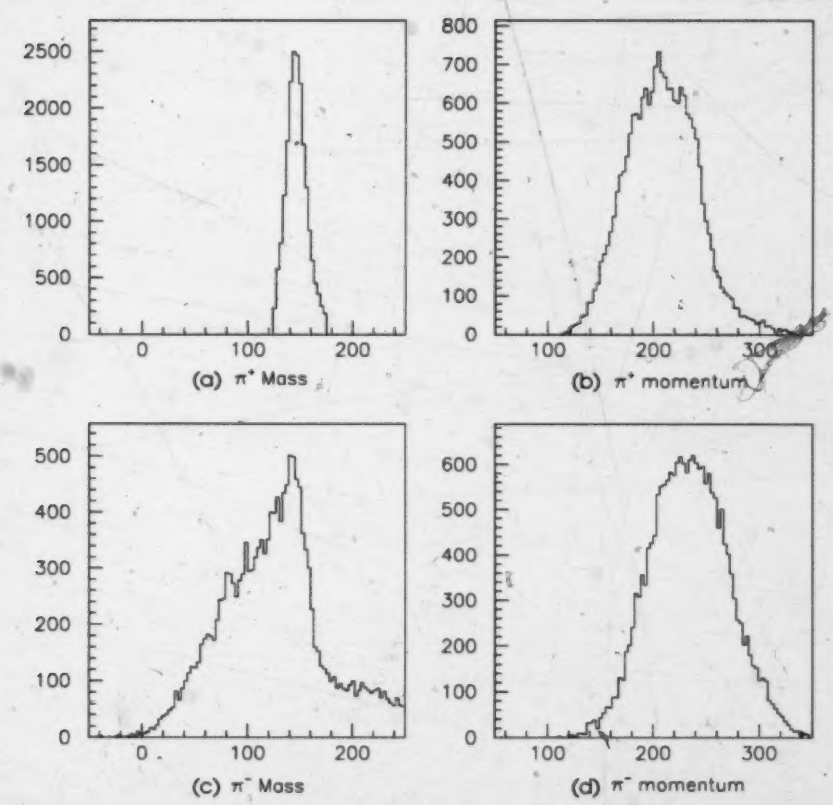

Figure 4.10: Mass and momentum spectrum for events surviving all cuts. The distinct $K_{\pi 2}$ peak is removed from the π^+ momentum plot. Also removed is the low mass electron peak in the π^- mass plot.

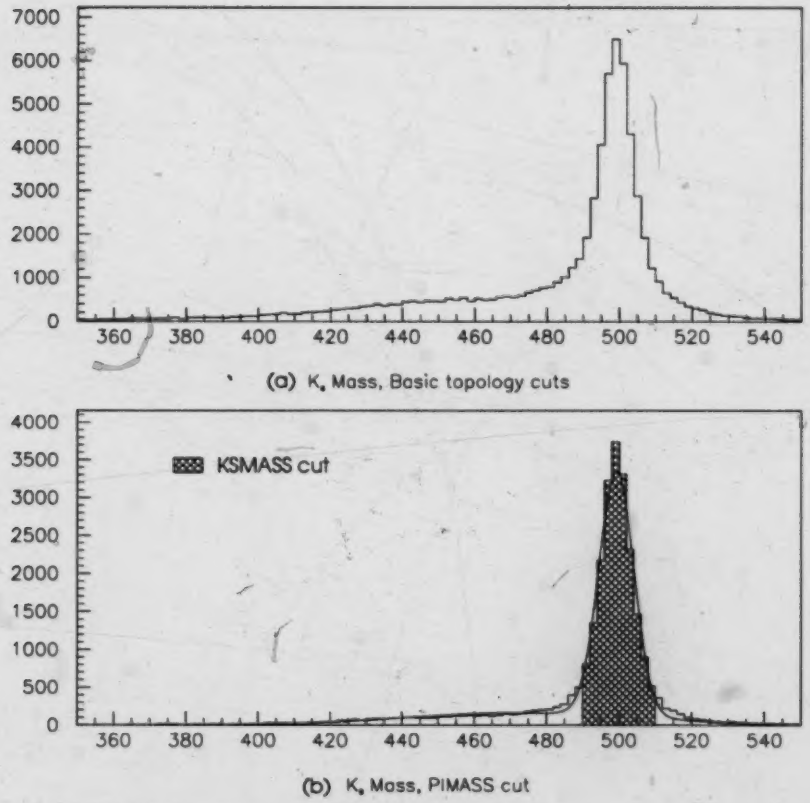

Figure 4.11: K_S^0 mass spectrum before and after cuts.

outward into the range stack where it will be stopped. Such an electron would be picked up by the UTC and RS track fitting routine and classified as a negative second track. The basic topology cut will be unsuccessful in distinguishing the pions and electrons. Photon conversion seems to be a rather common occurence in this trigger setup based on the π^+ momentum plot in Fig. 4.9b. The sharp peak at 205 MeV/c is plain evidence of this phenomenon. Mass measurement for these electron tracks yielded a lower peak around 30 MeV/c^2 in the mass plot for the π^-. The electron mass peak is not centered around 0 MeV/c^2 since we assumed a pion particle during the reconstruction and also the mass calculation. This high electron mass peak can also be attributed to the elctron showering within the scintillators. An example of the $K_{\pi 2}$ with photon conversion event is shown in Fig. 4.12.

The positron signal is observed if we require two positive tracks in the selection. Such a plot is shown in Fig. 4.13. The positron mass peak is not centered at zero because a pion hypothesis was used in the calculation. The negative track mass spectrum from the $+-$ track combination in Fig. 4.9c seems to show a broad peak centering around 30 MeV/c^2. The electron signal is not as distinct as the e^+ due to the contamination from π^- nuclear interaction.

Three Body Decays

For three body decays involving three charged particles, the available kinetic energy has to be shared by the three particles all of which will undergo dE/dx losses in the target plus bending by the magnetic field. As a result, it becomes unlikely for any of the decay particles to have enough momentum to reach the RS after traversing the target. Hence, only events from a very restricted corner of the phase space can survive the trigger. In the events satisfying the trigger, a large fraction of the available kinetic energy is carried away by the two tracks that give the T·2, leaving the third track with very little energy. In addition, the kaon needs to be close to the edge of the target letting the two particles escape the target before losing too much energy. After escaping the target, one of the particles must have enough energy to reach layer 6 of the RS. For kaon decay-in-flight, relativistic boosting will aid one of the pions to reach the RS.

It seems highly unlikely that both $K^+ \to \pi^+\pi^+\pi^-$ and $K^+ \to \pi^+\pi^0\pi^0$ will become a major background. If the $K_{\pi 3}$ does survive the trigger, it would most likely be a single track event, with the two-track event highly suppressed. Semileptonic decay modes, K_{e3} and $K_{\mu 3}$, that involved emission of neutrino will have a broader phase

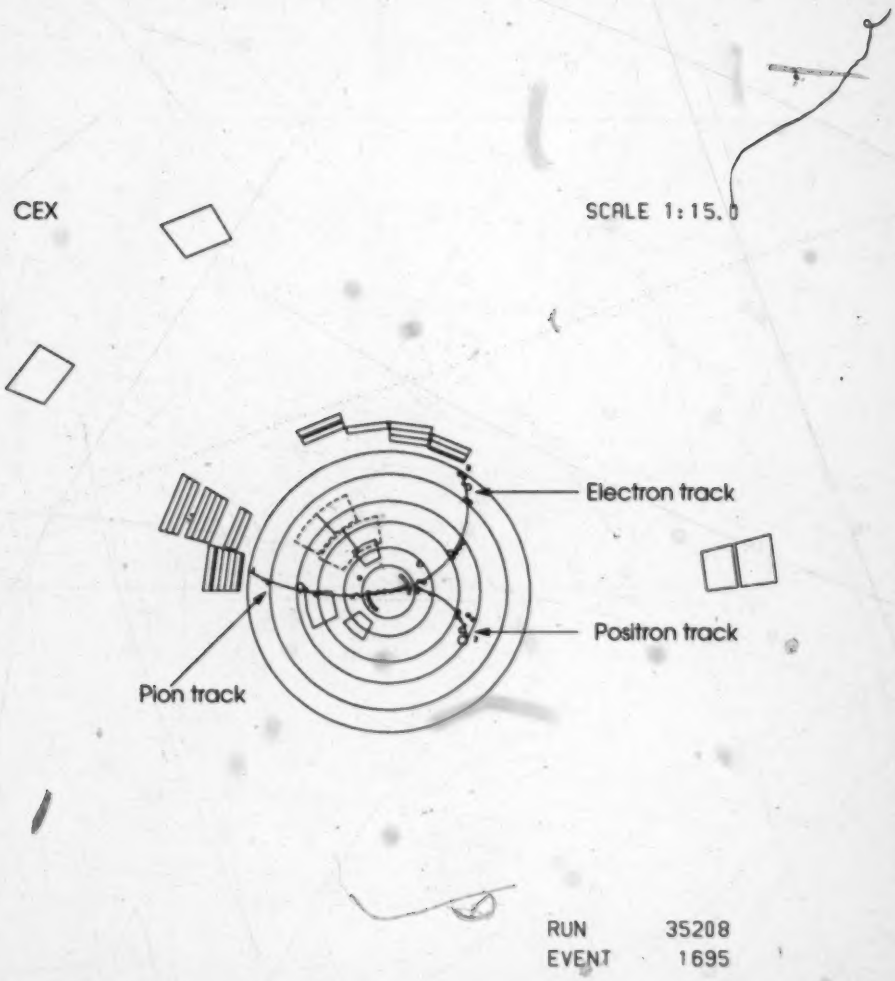

Figure 4.12: A $K_{\pi 2}$ background event. The curvature of the $e^{\pm}$ tracks are much bigger than the π^+ track. In this case, the e^+ reaches Superlayer 2 and annihilates. The electron is able to travel all the way to the RS counter.

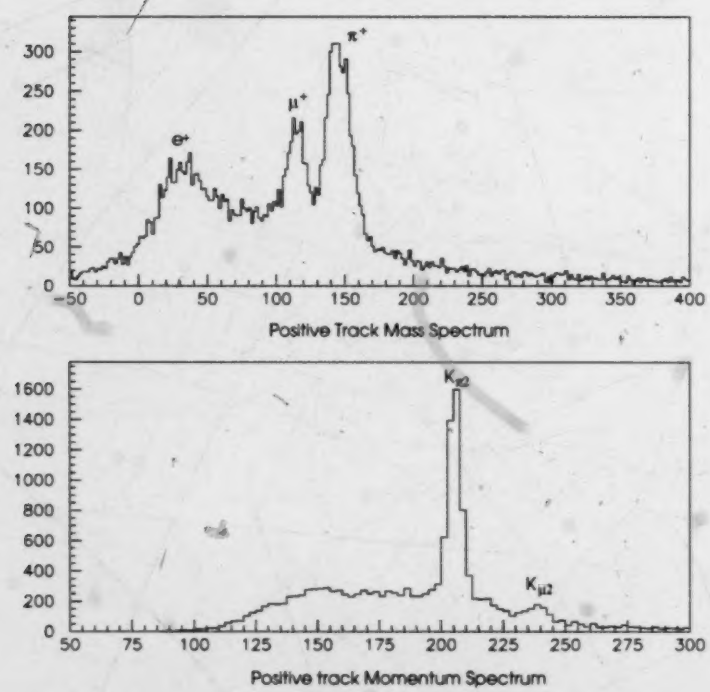

Figure 4.13: Mass and momentum distribution for the ++ track. Distinct mass peaks from π, μ, and e can be seen. The broad peak at low momentum is from the positrons.

Decay Mode	Acceptance	Background Estimate
$K_{\pi 2}$	3.43×10^{-3}	40
$K_{\pi 31}$	4.04×10^{-5}	2
$K_{\pi 32}$	3.05×10^{-5}	3
$K^+_{\mu 3}$	2.85×10^{-4}	8
K^+_{e3}	1.83×10^{-4}	5

Table 4.2: Acceptance for possible background.

space that could survive the trigger. These modes would require the π^0 Dalitz decay to produce the second charged track. Again relativistic boosting will give the e^+e^- enough energy to survive the RS trigger requirement.

Monte Carlo simulations were performed to measure the contributions of these decay modes in the CEX sample. The workings of UMC is discussed elsewhere in Section 5.1.1. The trigger used in the simulation is the CEX K^0_S trigger. The decay mode is then selected and simulation is done using the CEX trigger configuration. UMC, in its usual mode, will just simulate K^+'s decaying at rest. In order to simulate K^+'s decay-in-flight, the K^+ is moved an equivalent 50 MeV range upstream in the target. Then the K^+ is allowed to propagate in the target undergoing dE/dx energy loss or decay-in-flight. This 50 MeV pull-back mode is needed since UMC cannot properly simulate the full passage of the K^+'s starting from the beam element to the face of the target. The daughter particles resulting from the K^+ decay will be assigned the correct kinematic values. These daughters will then be propagated in the detector, undergoing ionization energy loss or decay. The acceptance for each decay mode is listed in Table 4.2. As expected, the $K_{\pi 3}$ decay modes are highly suppressed and could be safely neglected. The two semileptonic decay modes have a larger acceptance in the CEX trigger.

π^- Nuclear Interaction

Though nuclear interaction of π^- is not a background, this process added a layer of complication to the negative track signal. From kinematics, a two-particle decay has δ-function-like momentum peak for both particles. Such an effect is observed for the π^+ mass (Fig. 4.9a) spectrum whereas the π^- spectrum (Fig. 4.9c) seems to be a convolution of a peak around 150 MeV/c^2 with a broad peak around 30 MeV/c^2. Interestingly, there seems to be a cutoff at the π^- mass peak, suggestive of processes

involving pions.

Electron would contribute partially to this broad 30 MeV/c peak. Another cause for this downshift in the π^- mass spectrum is the π^- nuclear interacting with the RS material, particularly π^--absorption. Details on this subject matter will be deferred until Section 5.2.3. Generally, after absorption, a whole variety of particles like protons, deuterons and alphas are emitted. The heavily ionizing particles are usually unobservable in the RS, hence the RS track will end abruptly at the point of absorption. Absorption leads to shorter RS track range as well as a smaller energy measurement associated with the negative track. In such occurences, the π^- mass will be shifted up as indicated by the high mass tail in Fig. 4.9d. On the other hand, if neutrons are emitted in the absorption process, they will excite other nucleons within the carbon atom, resulting in the emission of additional low-energy neutrons and protons. This process is called nuclear evaporation. The π^- would then deposit a considerable amount of energy in its stopping counter and thus look like a lighter particle when its kinetic energy is compared to the momentum. The scenario is different for the π^+. At low energy, the π^+ decay probability is much higher than the absorption probability. Consequently, the π^+ will just lose its energy in the range stack and decay into a muon without undergoing the complicated absorption process. This explains the distinct π^+ mass peak in Fig. 4.9a.

4.3.2 Basic Topology Cuts

Since the interaction energy calibration curve is only valid for K^+'s with B4 pulse height between 1.8 and 3.2, events outside this B4 pulse height are removed. The cuts are:

- B4DEDX: 1.8 < `B4ABM2` < 3.2. Choose K^+ that has a valid energy calibration based on Fig. 4.6.

The second set of cuts simply reinforce the topology of the CEX events.

- TRKCUT: `NSECOND` = 2. This requires the reconstructed events to have two charged tracks.
- CHARGE: `CDC(1)`×`CDC(2)` < 0. Also requires the two tracks to be oppositely charged.
- DELCOB: |`tpi-tk`| < 2. Reinforces the $\overline{\text{DELCO}}$ offline. This will only select events that decay promptly.

Events derived from these cuts will serve as a basis for background studies and cut development. The mass and momentum distributions for this sample are shown in Fig. 4.9.

The mass of each charged track is calculated by using

$$\texttt{MPI}_i = \frac{(\texttt{pdc}_i^2 - \texttt{erd}_i^2)}{2 \times \texttt{erd}_i} \tag{4.5}$$

with i as the index for the charged track, **pdc** momentum from UTC, and **erd** the total unsaturated energy in the RS.

The total momenta of the tracks are calculated using the target ranges of individual tracks extrapolated back to the kaon stopping position. Using the momenta of the charged tracks, the invariant mass of the parent K_S^0 for a two-pion hypothesis is calculated using

$$\texttt{MKS}^2 = 2m_\pi^2 + 2\left[\vec{P}_1 \cdot \vec{P}_2 + \prod_{i=1,2} \sqrt{P_i^2 + m_\pi^2}\right] \tag{4.6}$$

The invariant mass plot is shown in Fig. 4.11. A peak at 500 MeV/c^2 which corresponds with the K_S^0 mass is observed in the plot.

4.3.3 Target Cuts

In order to establish the fact that the K^+ produced at least two charged particles, it is required that the same kaon fibers be found independently for both extrapolated UTC tracks. There $K_{\pi 2}$ decays of two simultaneous kaons, for example, can be eliminated.

- TGKAON: Remove events where the kaon blob are different for the extrapolated UTC tracks.

As mentioned earlier, the photon conversion from a $\pi^0 \rightarrow \gamma\gamma$ decay is a major source of background in the CEX trigger. With a π^0 lifetime of 8.4×10^{-17} sec, the π^0 conversion is guaranteed to occur in the target. In order to reduce the number of such events, connectivity between pion track cells and kaon blob as well as continuity of hit cells along each of the pion tracks is required.

- TGQUAL: LIKE_SW > 3.2 or LIKE2_SW > 2.3. Target quality cut.

The cut above ensures a proper target track reconstruction is performed for both tracks. SWATH determines which of the target fibers are the pion fibers by assigning a

likelihood to each fiber based on time, distance-from-swath, and energy in that fiber. SWATH then combines the likelihoods of all the pion fibers to form two variables. The first, LIKE_SW uses time, distance-from-swath and energy information. The second, LIKE2_SW only uses distance-from-swath. LIKE2_SW is useful for tagging events with a perfectly good pion track in the target but a mismeasured UTC track that does not match well with the target pion track.

The next target cut serves to remove events where lots of gamma fiber activities are observed.

- TGDCVT: TGAMMA>1 and sum of the gamma fibers' energies TEGAM > 3 MeV. Target photon veto cut.

The extra gamma activities have a few sources. Usually, the existence of cluster of gamma fibers with high energy hits away from the swath is caused by a second kaon entering the target. Gamma fibers with lower energy may be due to pion scattering into the target. A more common source of gamma fibers with low energy is the positron from from π^0 photon conversion either annihilating or curling back into the target without making into the UTC or RS. This cut serves to remove events where the e^+e^- pair is observed in the target.

4.3.4 Kinematic Cuts

So far, the cuts applied only select events with proper track reconstruction in the RS-UTC-TG systems. Next we will apply kinematic cuts to select out the K_S^0 decay.

- KSMASS: |MKS-500| < 10.
- PIMASS: |MPI-150| < 25.

The KSMASS cut will select events where the invariant mass calculated from the tracks' momentum is consistent with the K_S^0 mass. Background like Dalitz decay or any three-body decay will not reproduce the right invariant mass measurement due to their phase space distribution.

The PIMASS will only select events where the positive tracks lie under the π^+ mass peak. The mass cut is very effective in removing the K_{e3} and $K_{\mu 3}$ background since the positive track for these decay modes is either μ^+ or e^+. No mass cut is applied to the negative track since the π^- mass spectrum suffers ambiguity arising from nuclear interaction and Dalitz decay. The mass and momentum distribution for

the sample passing all the cuts are shown in Fig. 4.10. A few noticeable changes are observed in contrast to Fig. 4.9. The π^+ momentum peak at 205 MeV/c is effectively removed. The π^- mass spectrum does not exhibit any low mass peak around 30 MeV/c^2, but rather has a monotonic increasing structure as expected from the excess energy deposited by nuclear absorption.

As a cross-check, illustrated in Fig. 4.14 is the momentum of the π^+ and π^- plotted against the reconstructed K^0_S invariant mass. A cluster is observed at 200 MeV/c for the π^+, while a long smear starting from 50 MeV/c is seen in the π^- scatterplot. The π^+ cluster is coming from the $K_{\pi 2}$ decay and the π^- candidates in the smear are electrons from the π^0 decay. The same region is plotted after all cuts are applied. The cuts seem to have removed the $K_{\pi 2}$ contamination from the sample. The same procedure is also performed on an UMC data set where the backgrounds are included. This is shown in Fig. 4.15.

4.3.5 CEX Spectrum

The CEX spectrum obtained after applying the cuts is shown in Fig. 4.16. As a form of validation, the opening angles of the CEX events for each interaction energy are plotted in Fig. 4.17. Most of the low energy events do indeed have a back-to-back decay track; while the higher energy events experienced relativistic boosting, hence a change in the opening angle.

The trend in the stopping position distribution is also in agreement with the physical nature of CEX interaction. The direct correlation between the stopping position and cross-section is what will be used to extract the cross-section from the data. In the next section, the different corrections, efficiencies, and normalization calculations will be presented in detail.

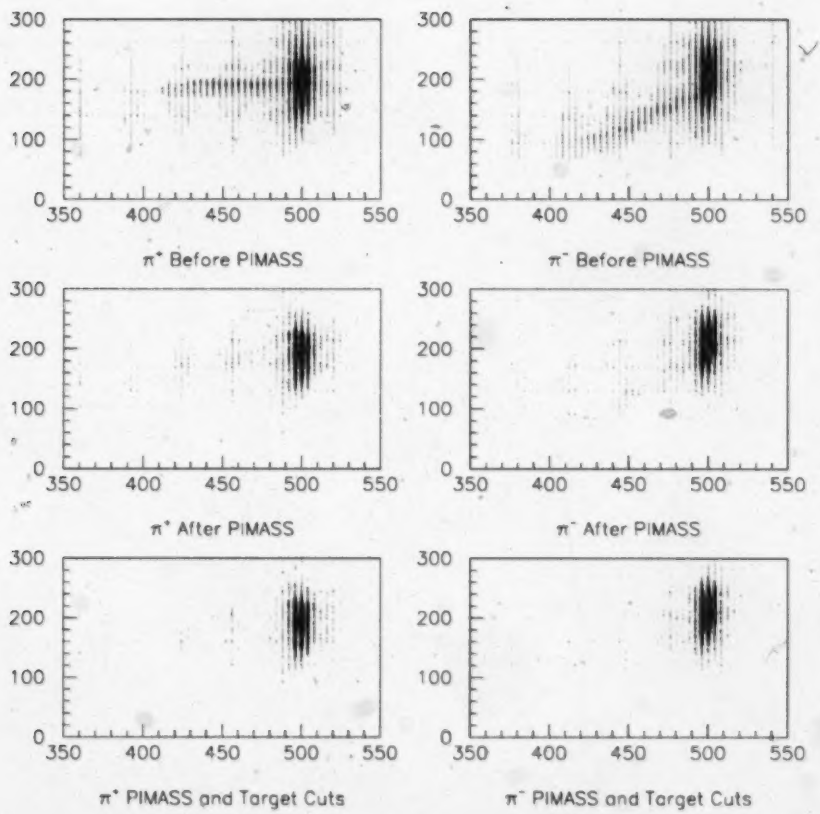

Figure 4.14: Removal of $K_{\pi 2}$ background using **PIMASS** and target cuts. Shown are scatterplots of M_{ks} vs P_{π}. With a combination of target cuts and the mass cut, $K_{\pi 2}$ background has been removed from the sample.

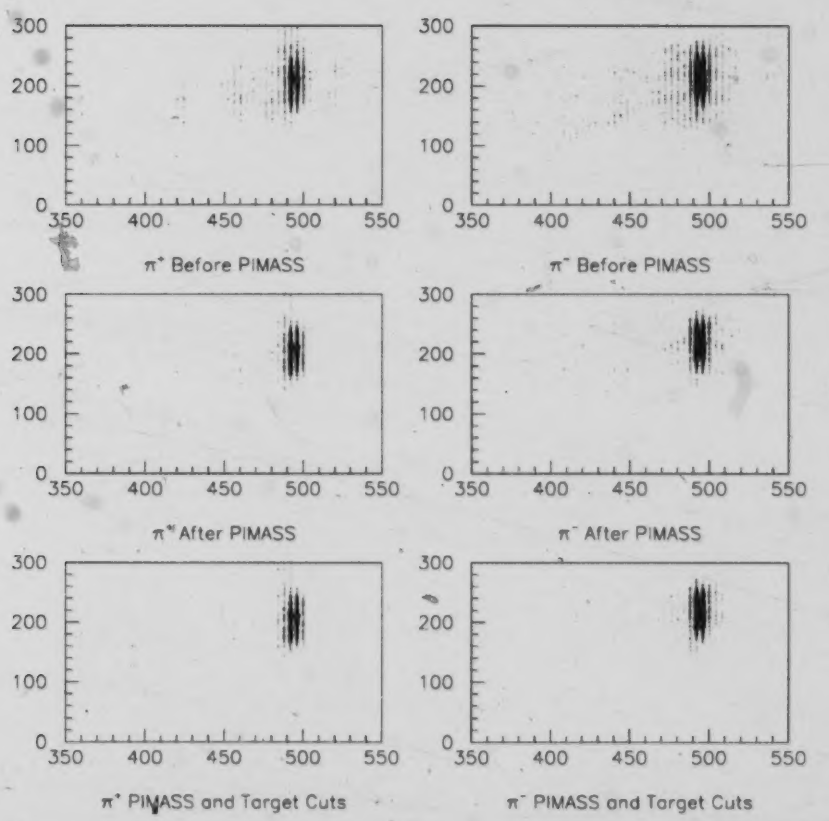

Figure 4.15: Scatterplots of UMC data before and after cuts. Included in this data are the different type of backgrounds.

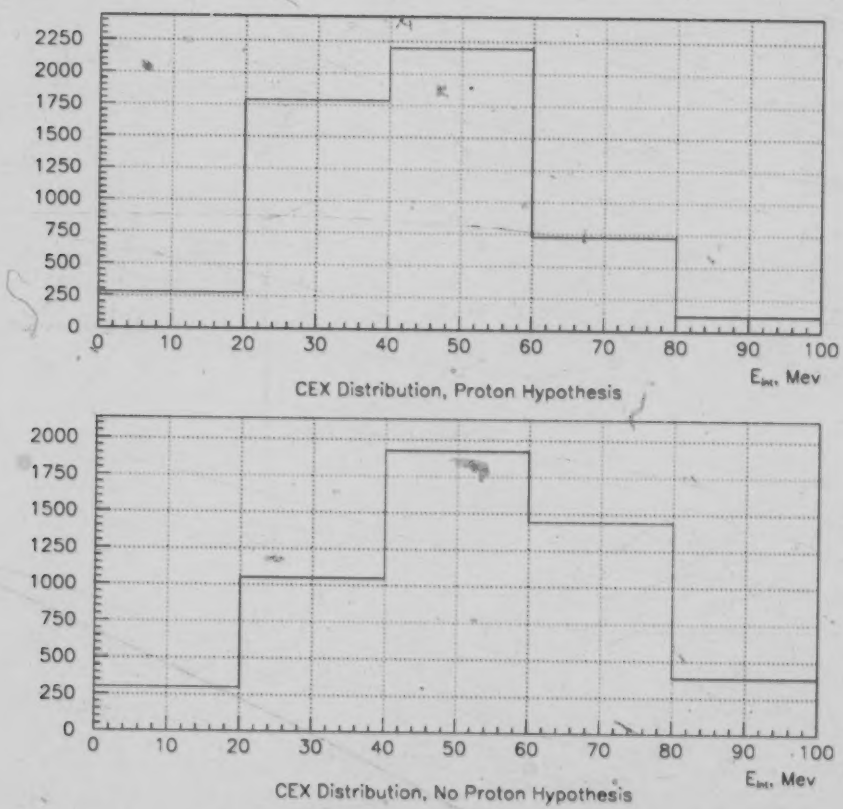

Figure 4.16: CEX event distribution for the two hypotheses at different interaction energy. This is the raw distribution without any acceptance losses correction. The spectrum has been downshifted after the proton energy correction.

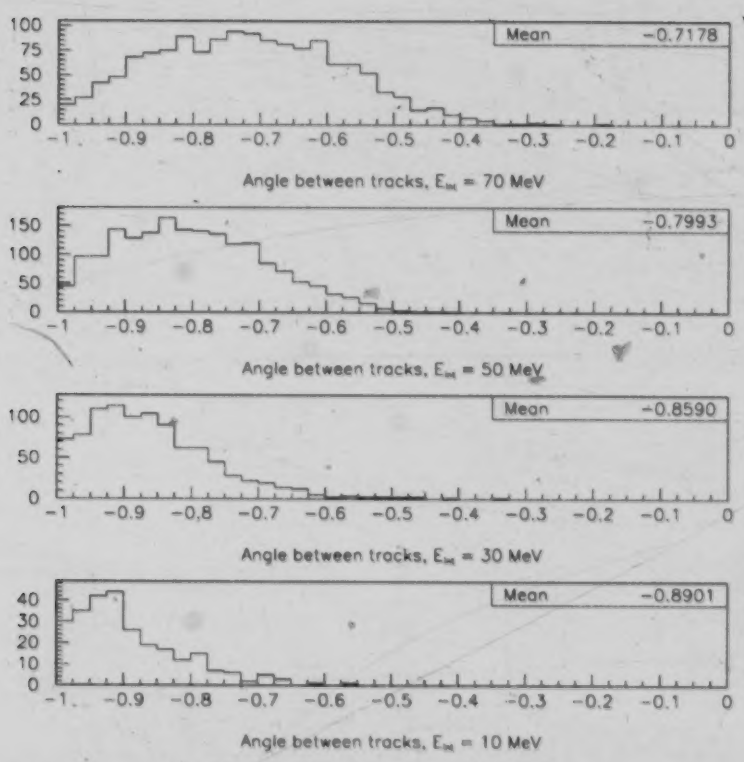
Mean −0.7178
Angle between tracks, E = 70 MeV
Mean −0.7993
Angle between tracks, E = 50 MeV
Mean −0.8590
Angle between tracks, E = 30 MeV
Mean −0.8901
Angle between tracks, E = 10 MeV

Figure 4.17: Opening angles between the $\pi^+\pi^-$ tracks for each interaction energy. Plotted is actually $\cos\theta$. For low energy interaction, a clear back-to-back decay of the K^0_S is observed. The existence of the tail is due to relativistic boosting.

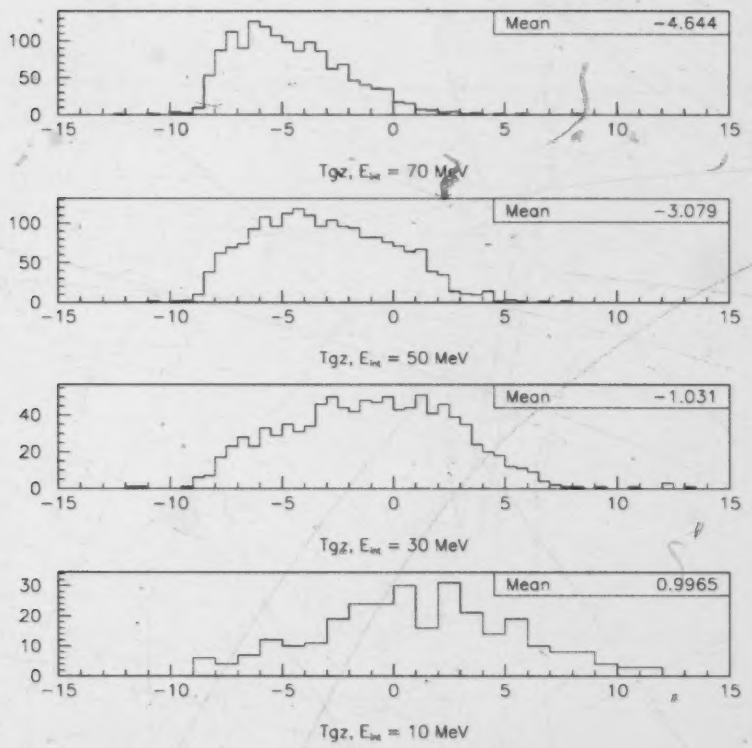

Figure 4.18: Stopping position of CEX kaon in the target. Note the shift in the mean stopping position. The shift is correlated with the cross section of the CEX process.

Chapter 5

Acceptance Measurement

To derive the cross section from the CEX events observed, one needs to know:

- The number of kaons that entered the target during the run, N_{KBlive}.
- The fraction of those kaons that underwent CEX and survived the trigger and offline analysis. This is the acceptance.

The probability, P, of an interaction for a given energy is:

$$\begin{aligned} dP &= \frac{I_{cex}}{I_o} = \sigma(E)nx \\ \text{or } \sigma(E) &= \frac{I_{cex}}{I_o nx} \end{aligned} \tag{5.1}$$

with $\sigma(E)$ being the total cross-section at the energy, I_{cex} is the number of particles undergoing CEX, I_o is the number of particles, n is the density of target nuclei, and x is the thickness of the target in cm. The ratio of I_{cex} and I_o in this experiment is given by:

$$\frac{I_{cex}}{I_o} = \frac{N_{CEX}(E)}{N_{KBlive} \times f_s(E) \times A_{tot}(E) \times \text{BR}} \tag{5.2}$$

where BR is the branching ratio of $K_S^0 \rightarrow \pi^+\pi^-$ and is equal to 0.686; $N_{CEX}(E)$ is the number of events in each energy bin; $A_{tot}(E)$ is the total acceptance for that particular energy bin; and f_s is the normalization factor to correct for the K^+ flux. A_{tot} is broken into different factors. Most of the acceptance factors are valid globally for all interaction energies. A few factors will vary with the energy due to the nature of the factor considered, giving rise to the energy dependence of A_{tot}.

Given a large sample of $K_S^0 \to \pi^+\pi^-$, every cut applied to the sample will remove some real events. This is an acceptance loss, and all the losses must be properly added up in order to translate the events observed into the cross section. If the Monte Carlo simulation is perfect, the task of calculating A_{tot} would be fairly simple. We could generate a sample of N_0 $K_S^0 \to \pi^+\pi^-$ CEX events, run through the online trigger simulation and offline analysis by applying all cuts to this sample, and count the number of survivors N for each interaction energy. The acceptance would simply be N/N_0. However, UMC falls short in many ways to achieve such perfect simulation. There are issues with timing and energy resolutions, and nuclear interaction processes that are not well represented in the program. Reliance on UMC should be kept to the minimum. UMC is used to measure the acceptance of cuts that depend on the kinematics of $K_S^0 \to \pi^+\pi^-$, *i.e.*, the online trigger acceptance and offline fiducial volume acceptance. Effects that depend on nuclear interactions of $\pi^\pm$ will be measured using the data. Presented in the following sections are the detailed calculations of A_{tot} and f_s.

5.1 UMC based Measurement

Monte Carlo is used to measure the following:

- The Level 0 trigger acceptance loss, A_{trig}. It measures the geometrical acceptance of the detector, particularly the two-track acceptance. This does not include the online delayed coincidence requirement in the trigger, nor does it include the online photon veto cuts. These are measured with data.
- Target z biasing correction in the trigger, A_{tgz}. Serves to remove the biasing of the trigger acceptance along the target z.

5.1.1 Trigger Acceptance, A_{trig}

The CEX simulation is a new feature added into UMC. A beam distribution file whose information contained: a list of real target interaction points (`tgx,tgy,tgz`), reconstructed K_S^0 momentum, individual hit times and energy deposits for the kaon fibers, B4 hit positions, B4 timing, and B4 pulse heights are first generated from the CEX data. The CEX Monte Carlo would assign these values to a K_S^0 and place it in the UMC stack. Once in the stack, the K_S^0 is forced to decay into 2π and the

Requirement	N_{passed}	Acceptance
KB	293558	–
one T·2	182133	0.620
2 T·2	81964	0.450
($\overline{\text{DELCO}}$)	81964	1.000
Reach layer 6 or 7	80082	0.977
(Endcap Veto)	80082	1.000
(Barrel Veto)	64902	0.810
Pass μ veto	54297	0.836
A_{trig}		0.1850±0.0017

Table 5.1: CEX trigger acceptance factors. Those in parentheses are not counted here but are measured with data.

daughter pions will propagate through the detector simulation. Only the π^+ nuclear interaction code is enabled in the Monte Carlo. The π^- nuclear interaction is turned off to avoid any improper simulation of π^- nuclear interaction. In this manner, all π^+ corrections are taken care off by the Monte Carlo, while the π^- corrections can be measured using data which is more accurate. A comparison between UMC events and data can be found in Appendix A.

The Level 0 trigger is simulated and those events passing the trigger are written to disk. The trigger acceptance is calculated by counting the numbers of events passing various trigger requirements. The results are summarized in Table 5.1. From Table 5.1, A_{trig} is not exactly the $K_S^0 \to \pi^+\pi^-$ trigger survival fraction. The reason is that both the online $\overline{\text{DELCO}}$ and the photon veto subsystem (Endcap and Barrel Veto) depend critically on the details of the trigger timing or subsystem efficiencies, and will be measured separately with data. The trigger acceptance for CEX events is 18.5 %. The big drop in trigger acceptance occurs at the 2(T·2) requirement. Remember that the detector is optimized to detect the single track $\pi^+\nu\overline{\nu}$ event; with the beam momentum tuned to provide stopped kaon with the maximal T·2 coverage. It is hardly a surprise that the T·2 acceptance is low for the CEX trigger.

5.1.2 Target z correction, A_{tgz}

Recalled from Section 3.3, the signal from the I-counter which defines the fiducial region of the detector, is part of the DELCO and T·2. Events not hitting the IC

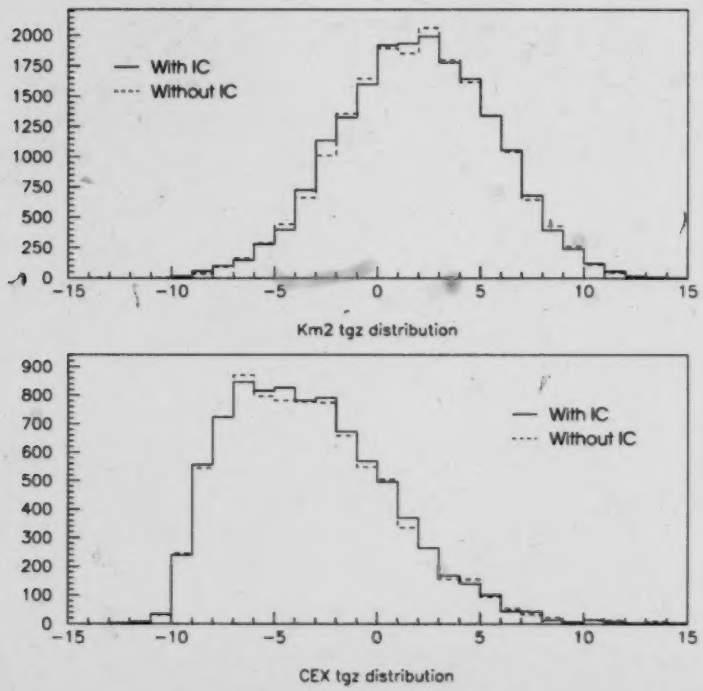

Figure 5.1: Kaon stopping distribution with zero beam offset. No discernable differences in acceptances are found in cases with and without IC for km2 and CEX.

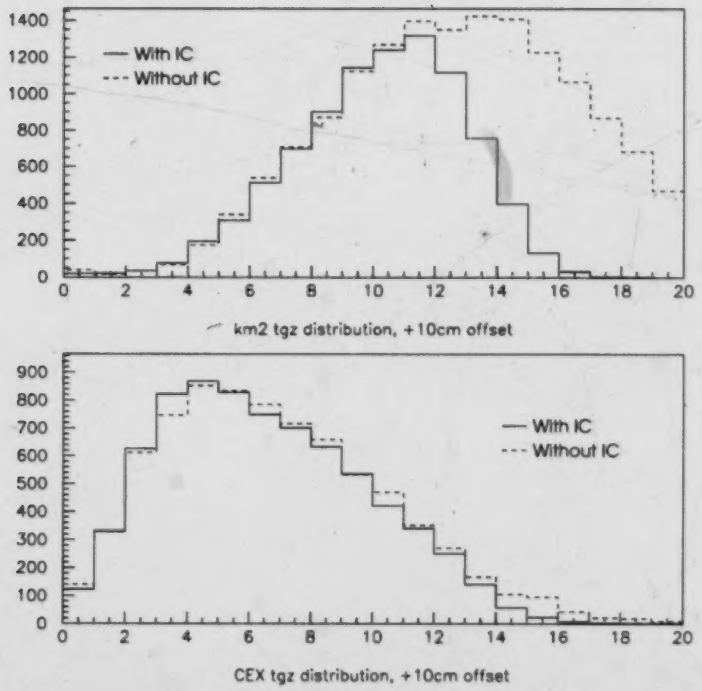

Figure 5.2: Kaon stopping distribution with offset = +10 cm. A drop in acceptance is observed for km2 when **tgz** > 14 cm. The acceptance drop in CEX is not as drastic as the km2 case.

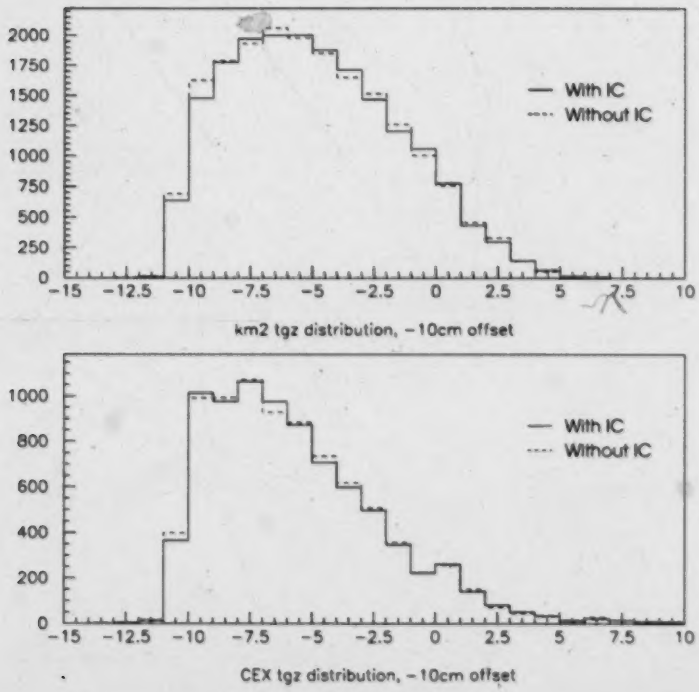

Figure 5.3: Kaon stopping distribution with offset = -10 cm. Again no obvious differences in acceptances are found in cases with and without IC for km2 and CEX.

will be lost since they cannot satisfy the basic trigger definition. In essence, the IC fiducial region can only observe a certain phase space for any given K^+ decay mode. The IC acceptance has been optimized such that the acceptance is greatest at the center of the target for stopped kaon. This is to facilitate the $\pi^+\nu\bar{\nu}$ search where the beam is tuned to stop at target center. CEX events, though, do not have the luxury of this acceptance optimization. CEX occurs throughout the target and hence suffers from a trigger biasing introduced by the IC. Events occuring close to target face or deep in the target will tend to be missed since the IC fiducial region is small, whereas events occuring at target center will be readily triggered.

The usual UMC simulation includes the IC as part of the trigger simulation. Therefore, a modified UMC is created where the IC is removed from the trigger definition. Simulations with and without IC are performed for both CEX and $K_{\mu 2}$. The $K_{\mu 2}$, a single track event, is used to validate the UMC output. An offset can be applied to the kaon stopping position in the beam file. Below is the summary on the simulation results:

Beam offset = 0.0 cm

In this setting, the simulation is carried out using the default CEX and $K_{\mu 2}$ beam files. The stopping distributions with and without IC for both event types are shown in Fig. 5.1. In both cases, the acceptances across **tgz** are identical simply because the beam file used in event generation is inherently IC-biased. Inclusion of the IC bit reduces the statistics in the target region of interest. To enhance the statistics, one can simply apply an offset to the kaon stopping position in the beam file.

Beam offset = +10 cm

The overall kaon stopping position is shifted 10 cm downstream into the target. Results are shown in Fig. 5.2. As expected for the $K_{\mu 2}$ case, the acceptance beyond 14 cm drop drastic when the IC is required. The drop in acceptance is not as dramatic for the CEX case since the CEX is a two-track decay. If one of the track misses the IC, the second track would still hit the IC and hence pass the trigger.

Beam offset = -10 cm

Here, the stopping position is shifted 10 cm upstream to the face of the target. Results are shown in Fig. 5.3. The sharp dropoff at **tgz** $\approx$ -11 cm marks the beginning of

the target. By definition, no decay should occur before this region unless it is from the beam line. The acceptance loss is not as high as the +10 cm offset since the IC actually extended 0.635 cm out from the target. Particle travelling backward can still hit the overhanging part of the IC.

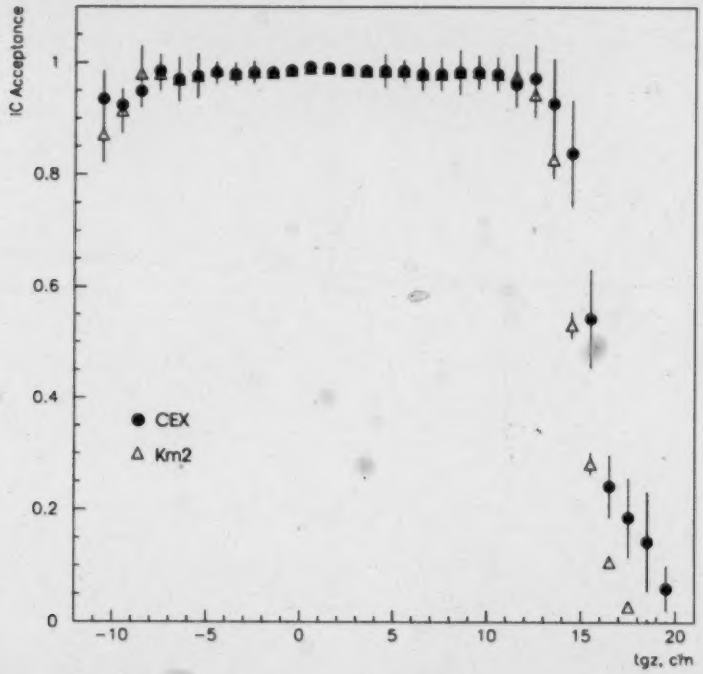

Figure 5.4: IC acceptance as a function of tgz. The acceptance is identical for km2 and CEX for most part of the target length, except at the beginning and downstream end of target. The CEX acceptance is higher in both regions due to its two-track topology.

The IC acceptance as function of tgz is plotted in Fig. 5.4. Overall, the acceptance is identical for both CEX and $K_{\mu 2}$ except at the edges. The CEX acceptance is higher than the $K_{\mu 2}$ at both extreme ends due to its two-track topology. Noted too is that the CEX events occurring at this region have higher energy, hence the tracks tend to be forward peaked.

Cut	N_{passed}	Acceptance
Selection	1007	-
Offline $\overline{\text{DELCO}}$	881	0.8749
B4DEDX	835	0.9477
A_{cex}		0.8292±0.0013

Table 5.2: CEX event selection factor, A_{cex}.

Cut	N_{passed}	A
Selection	1503	-
TGQUAL	1433	0.9534
TGDCVT	1314	0.9169
A_{tt}		0.8742±0.010

Table 5.3: Target cut acceptance factor, A_{tt}.

5.2 Data based Measurements

5.2.1 Cuts' Corrections

As mentioned earlier in Sect. 4.3, the basic cuts to select good kaon event invertibly lead to some acceptance losses. Here we will attempt to correct for these losses using the data.

The kaon selection acceptance losses are measured using the km21 monitor data taken concurrently with the CEX. The results are summarized in Table 5.2. The target cuts' acceptance are measured using the $K_{\pi 2}$ data.

5.2.2 $\overline{\text{DELCO}}$ acceptance, A_{dc}

The online $\overline{\text{DELCO}}$ acceptance has to be measured separately since the UMC timing resolution does not replicate that of the real data. The $K_{\pi 2}$ monitor stream does not contain an online $\overline{\text{DELCO}}$ requirement. Contained within the $K_{\pi 2}$ monitor data are $\pi-$scattering (piscat) events which have prompt timing. $\pi-$scattering events are basically pions from the beamline scattering into the detector and satisfied the trigger. Since these pions are not a result of any kaon decay, their time of detection will be almost identical to the beam strobe timing, resulting in a prompt timing signature.

Piscat events from the kp21 stream are selected using these cuts [29]:

Cuts	N_{passed}	Acceptance
Selection	657	-
`ext(2)=0`	632	0.962
A_{dc}		0.962±0.008

Table 5.4: Online Delayed Coincidence Acceptance, A_{dc}.

- PVCUT, KINCUT, TDCUT : Remove the kp2 events.
- BWTRS, B4TRS, B4TD, CKTRS, CKTAIL, BHTRS, TGQUALT, TIMCON, TGZFOOL, EPITG, EPIMAXK, TGER, TARGF, DTGTTP, RTDIF, DRP, PHIVTX, PHIVTX2, OPSVETO, TGCCD, TGCCDPF, EIC, TIC, KIC, TGEDGE, TGGEO : These cuts served to remove kaon decay-in-flight and double beam background events.

The piscat selection will give the total number of prompt events, N_{prompt}. The logical bit, `ext(2)` = 1, represents a satisfaction in the DELCO trigger bit. For any prompt event, `ext(2)` would be in the low state or zero. Imposing `ext(2)` = 0 on the selected piscat would give the events that the trigger tagged as prompt events, N_{dcbar}. The ratio

$$\overline{\text{DELCO}} = \frac{N_{dcbar}}{N_{prompt}} \tag{5.3}$$

give the required value of A_{dc}.

5.2.3 Nuclear Interaction Corrections

The remaining calculations are attempts to measure and correct for the nuclear interaction that the pions experienced at different detector elements. Most of the efforts will be concentrated on understanding the nuclear interaction process for π^- since the probability of a nuclear interaction in the scintillators outweights the probability of decay. We will first describe the nuclear interactions of interest and then proceed to calculate the correction factors for the interactions.

First consideration is the radiative capture of π^- by ^{12}C:

$$^{12}\text{C} + \pi^- \rightarrow {}^{12}\text{B}^* + \gamma \tag{5.4}$$

Radiative pion capture usually generates a very hard gamma spectrum (> 60 MeV), followed by a slower emission of low energy β or γ from the de-excitation of ^{12}B*.

With a branching ratio of 1.67 ± 0.08 % for all π^- absorbed in nuclei, the radiative capture is a rather rare occurence. The dominant process is the absorption of π^- by the nucleus. If the absorption were to take place on a single nucleon (hydrogen), the reaction

$$\pi^- + A \rightarrow n + (A-1) \tag{5.5}$$

would result in a neutron with an energy of about 130 MeV. The neutron would carry away a momentum of about 510 MeV/c, but this high a momentum cannot be obtained from the Fermi motion of a single nucleon in the nucleus. The absorption normally takes place on a correlated proton-proton or neutron-proton pair in the nucleus. We can thus safely ignore the absorption on hydrogen and assume that all absorption occurs with the ^{12}C of the scintillators.

When absorption occurs with the ^{12}C, the nucleus will gain additional energy equivalent to that of π^- mass. At this point, the nucleus will be split into different fragments. The particles emerging could include neutrons, protons, deuterons, alphas, etc. These particles will carry away a large amount of the energy deposited by the π^-. The remains of the ^{12}C nucleus will de-excite by particle evaporation and γ-ray emission. Finally this unstable nucleus may decay by β emission or electron capture.

The π^- absorption is a rather complicated process, leading to a production of a wide variety of different particles. Detection of these end products is a non-trivial task considering the many different possible outcomes from the absorption process. The heavy charged particles like protons and deuterons are usually unobservable in the RS. This is due to the saturation effect within the RS scintillators[1]. Then, the π^- would appear to have disappeared before reaching its full range. Its RS energy measurement would then be downshifted when compared with its measured momentum in the UTC.

Photons associated with the absorption will be detected either by the RS or the photon veto system. If the photon energy is too high, this will lead to a veto of such event by the trigger. As for electrons, if detected, they will create a kink in the original π^- track. This may cause a failure in the RS track reconstruction software. Neutrons from the absorption process will be scattered and captured by the surrounding H or C atoms, forming an excited atom. The atom will de-excite through photon-emission. The photon signal will have a delayed timing compared to the original π^- track.

Effectively, π^- nuclear interaction introduces complications into the detection and

[1]Recall the same effect described in Section 4.2.2 for the proton energy correction

reconstruction of the negative track. The next few sections will be procedures employed to correct for the loss in data arises from π^- nuclear interaction.

5.2.4 K_S^0 Detection and Reconstruction Efficiency

The K_S^0 detection is inherently dependent on two factors, namely the detection and reconstruction efficiency of the $\pi^+\pi^-$ involved in its decay. The $\pi^+\pi^-$ tracks from data contain the complete picture of the different nuclear interactions (elastic, inelastic scattering, absorption process, etc) that the pions might undergo when they traversed the RS material. Some of these interactions cannot be simulated satisfactory by UMC. Hence nuclear interaction code is turned off during the simulation. Instead, the pions are merely allowed to propagate through the detector elements undergoing decays and ionization energy losses.

Bearing in mind the differences between the UMC and real data, we will proceed to calculate the detection efficiency of the K_S^0. Fig. 5.5 gives a schematic summary to the procedure. The CEX data is subjected to these conditions:

- TRKCUT
- CHARGE
- KSMASS

The resulting sample will be a set of properly reconstructed K_S^0 (or $\pi^+\pi^-$) events. By clustering the pions into their respective type and then imposing a PIMASS cut on the other track will yield the pion detection efficiency. As an example, we will examine the π^+ set after the selection. If the pion detection efficiency is perfect, imposing the PIMASS on the other track (π^- track) will have no effect whatsoever on the π^+ data set. Hence any missing events are due to the inefficient detection of pions. The efficiency as a function of P_π is plotted for π^+ and π^- in Fig. 5.6. The same procedure applied to the UMC data will yield the π detection efficiency for the detector. The plots give an average detection efficiency of 0.93 for both π^+ and π^- track. As for data measured efficiency, the value for π^+ hovers around 0.75, while π^- around 0.32.

Imposing PIMASS cut on both tracks on the UMC and real sample will yield: (i) a K_S^0 sample where the pion tracks suffer no ambiguity in their reconstruction; (ii) a K_S^0 sample containing all the complications of pion nuclear interaction that

E_{int}, MeV	A_{ks}	
	With Proton	Without Proton
90.0	$(4.07\pm0.42)\times10^{-3}$	$(8.59\pm0.73)\times10^{-3}$
70.0	$(8.32\pm0.45)\times10^{-3}$	$(13.99\pm0.98)\times10^{-3}$
50.0	$(21.87\pm1.12)\times10^{-3}$	$(24.82\pm1.49)\times10^{-3}$
30.0	$(42.59\pm3.41)\times10^{-3}$	$(35.79\pm2.14)\times10^{-3}$
10.0	$(39.69\pm3.17)\times10^{-3}$	$(46.15\pm3.70)\times10^{-3}$

Table 5.5: K^0_S detection factor, A_{K_s}.

might fool the detector and software. The ratio (after proper normalization) between the UMC and real data will give the K^0_S reconstruction efficiency. However, this reconstruction efficiency includes the 93% Monte Carlo π detection efficiency. Thus, the reconstruction efficiency is obtain by unfolding the π detection efficiency from the total efficiency, *i.e.*,

$$\epsilon_{recon} = \frac{\epsilon'_{recon}}{\epsilon_{\pi\ detect}(UMC)} \tag{5.6}$$

and the final K^0_S detection efficiency given by

$$\epsilon_{K_s} = \epsilon_{recon} \times \epsilon_{\pi} \tag{5.7}$$

The K^0_S reconstruction efficiency is plotted in Fig. 5.7. The ϵ_{K_s} obtained can be applied to the data as a correction factor. The acceptance factor at each interaction energy is given by Table 5.5

5.2.5 Online PV Acceptance

The CEX data set studied is collected with an online photon veto requirement. It should be noted that no offline photon veto cuts are applied on the data aside from the online PV requirement of $\overline{\mathrm{BV}+\mathrm{EC}}$. The online PV cut is probably the loosest cut available, while any application of offline PV cuts could easily remove good CEX event. The trigger requirement, though loose, would still cut out valid CEX events where the π^- interacting with the ^{12}C may produce hard photon that gets vetoed by the trigger. Here we will attempt to account for the losses due to these effects in the range stack.

A special run where the online PV is turned off is used in this occasion. Since the trigger has no photon veto requirement, $K_{\pi 2}$ events fooling the trigger made up a

Figure 5.5: Schematic diagram on the K^0_S efficiency measurement.

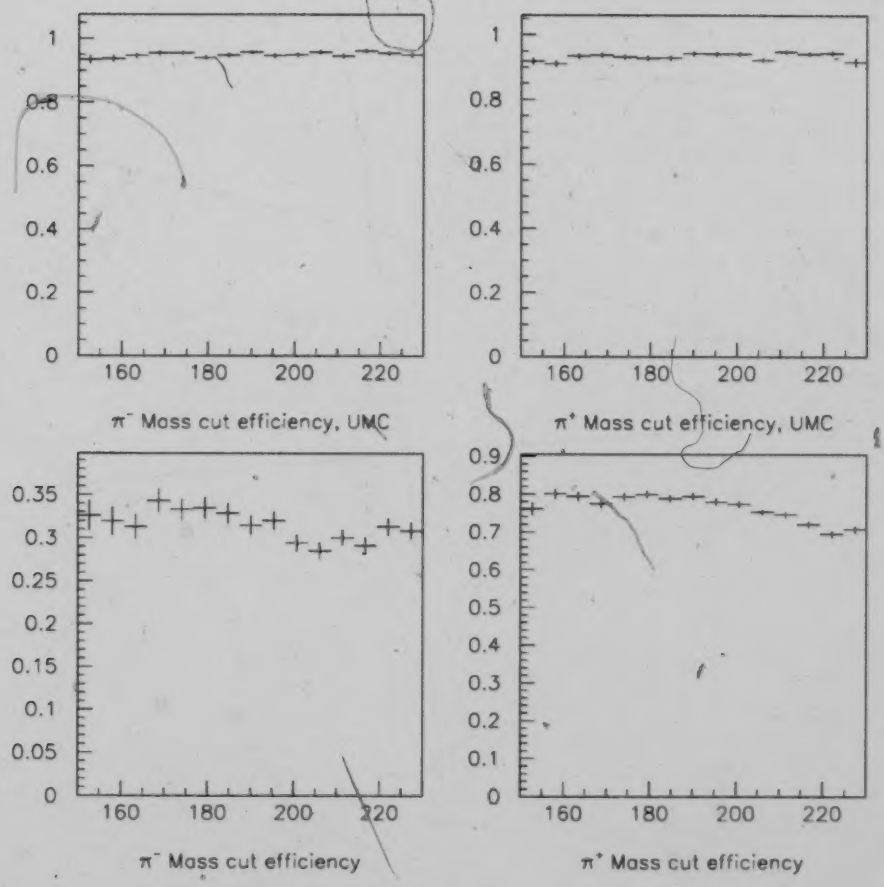

Figure 5.6: Detection efficiency for π^+ and π^- from the K^0_S and UMC data

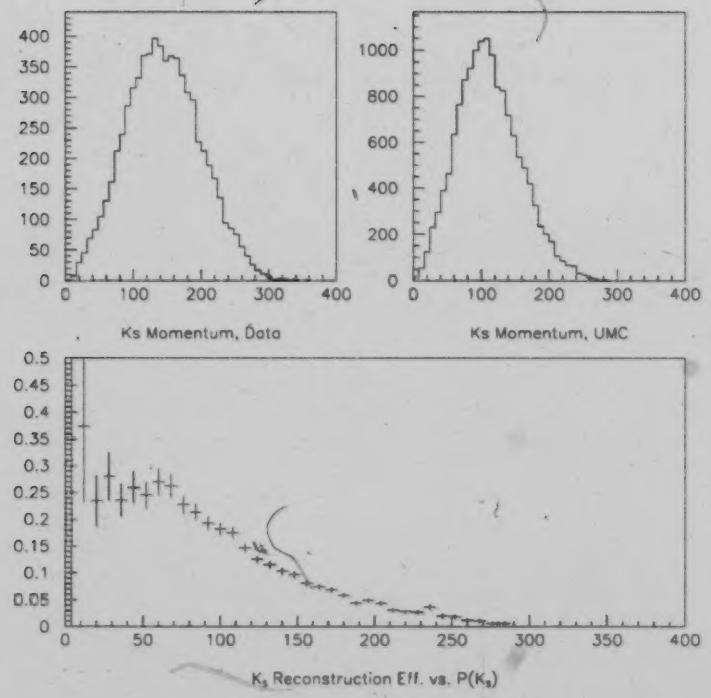

Figure 5.7: K_S^0 reconstruction efficiency as a function of its momentum.

E_{int}, MeV	A_{PV}	
	With Proton	Without Proton
90.0	0.8493±0.0323	0.8163±0.0079
70.0	0.8565±0.0130	0.8232±0.0103
50.0	0.8302±0.0080	0.8251±0.0088
30.0	0.8260±0.0090	0.8235±0.0118
10.0	0.8258±0.0229	0.8287±0.0245

Table 5.6: PV acceptance factor, A_{PV}.

large portion of the data set. To properly extract the PV acceptance, one must ensure that the $K_{\pi 2}$ contamination is minimized. Aside from measuring the PV acceptance, this background-rich data set has led to the development of the target cuts. A sample of clean CEX events is defined by the application of these cuts: KSMASS, PIMASS, TRKCUT, TGQUAL, and TGDCVT. Defining this sample as N_{cex}, it would contain all CEX events. The photon veto subsystems of interest in this study are the BV and EC which correspond to the logic variables **ext(4)** and **ext(5)** respectively. A logical ON bit for these variables signifies photon activity in the respective subsystem, while an OFF bit would mean no or below threshold photon activities. By imposing both PV logical bits to be off, *i.e.*,

$$(\textbf{ext(4)} = \text{OFF}) \text{ .AND. } (\textbf{ext(5)} = \text{OFF}),$$

only CEX events without photon activities will be selected, replicating the effect of the original trigger setup. The acceptance is then defined as:

$$A_{PV} = \frac{N_{off}}{N_{cex}} \tag{5.8}$$

The factor is plotted as a function of $\pi^+\pi^-$ momentum in Fig. 5.8 whereas the final PV acceptance factor for each interaction energy is given in Table 5.6.

5.2.6 Target Interaction Correction

It is possible for the π^- to interact in the target before reaching the UTC. In this case, only the π^+ will be detected and the event will either be vetoed by the 2(T·2) trigger or TRKCUT. It is very difficult to directly measure such an occurance in the target since the highly ionizing particles produced by the interaction will be undetectable.

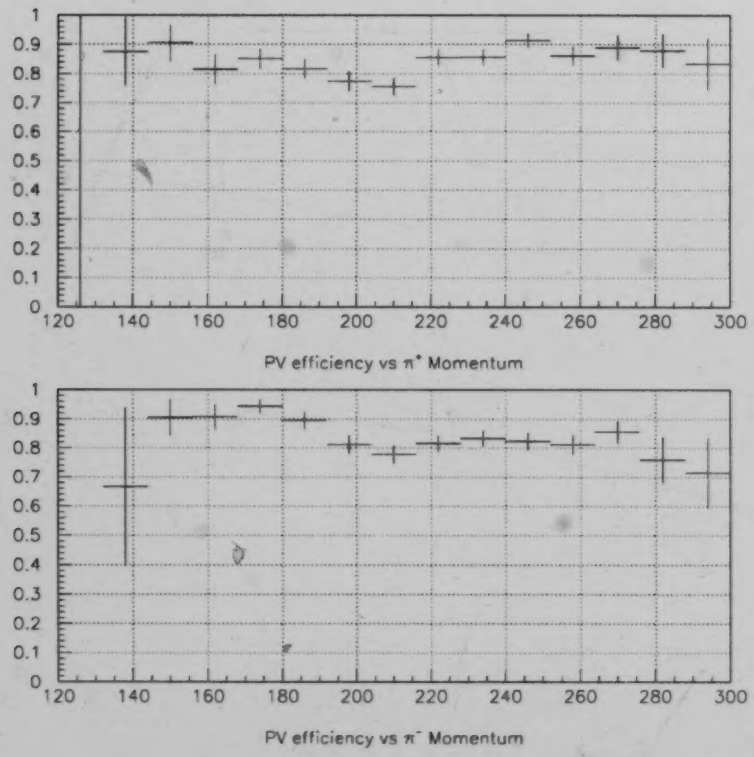

Figure 5.8: Online photon veto efficiency.

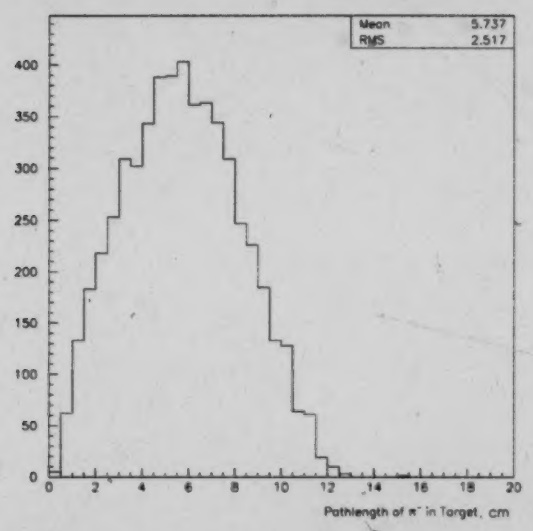

Figure 5.9: Pathlength of π^- in target. The average distance the π^- traverse in the target is around 7 cm.

The experimental values of the π^- total cross section at different momenta is plotted in Fig. 5.10. These cross-section values take into account all the possible interactions of the π^- with carbon atom. We define the initial flux as I_o and the final flux, I_f, the ratio of pions that undergo interaction is

$$\begin{aligned} \frac{I_f}{I_o} &= \frac{\sigma \rho N_o x}{A} \\ \text{or} \quad I_f &= \frac{\sigma \rho N_o x}{A} I_o \end{aligned} \tag{5.9}$$

where x is the pathlength the pion travelled in the target. The target pathlength distribution is shown in Fig. 5.9. For a π^- with momentum 200 MeV/c, the total cross section is 600 mb which corresponds to a 21% correction factor if the pion travel 7 cm in the target. Equation 5.9 is applied to every π^- to correct for the missing π^-. The correction factor at each energy is given in Table 5.7. These factors are inherently dependent on the momentum and pathlength distribution at each interaction.

E_{int}, MeV	A_{tcor}	
	With Proton	Without Proton
90.0	0.816±0.037	0.879±0.017
70.0	0.884±0.012	0.865±0.009
50.0	0.898±0.006	0.814±0.010
30.0	0.820±0.009	0.857±0.011
10.0	0.854±0.021	0.871±0.019

Table 5.7: Target nuclear interaction correction factor.

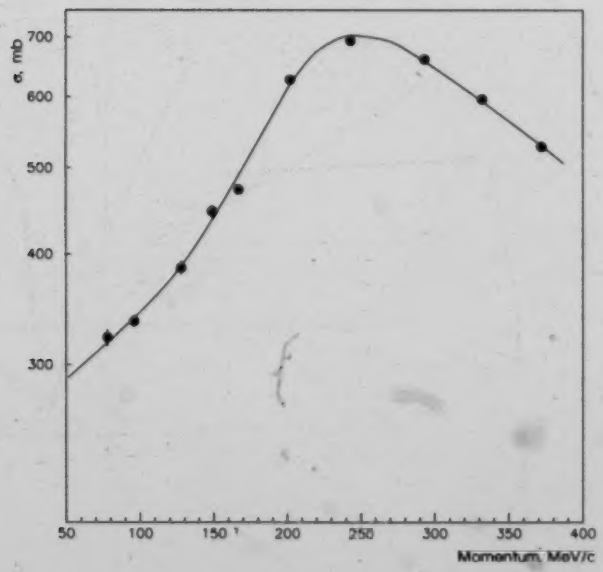

Figure 5.10: Experimental values of π^- total cross section with carbon[30, 31]. The solid line are hand-drawn.

Chapter 6

Kaon Flux Normalization

Going back to Equation 5.2, the term

$$\frac{N_{cex}(E)}{A_{tot}(E) \times BR}$$

represents the total number of CEX events produced in the data set. This term is now known since $A_{tot}(E)$ has just been completed in the previous section. What remains is the term, $N_{KBlive} \times f_s$, which will be the kaon flux normalization used to obtain the CEX cross-section.

It is worth pointing out the differences between a typical transmission measurement and our experiment. These differences, hopefully, will help clarify the strategy we have adopted to calculate the flux normalization and the cross section.

1. The target used in the transmission experiment is thin and well-defined, typically of a few mm in thickness. Our target is thick (20 cm!). The actual amount of material encountered by the K^+ varies according to its energy.

2. The energy or momentum in the transmission experiment is a well-known quantity, usually determined by the incoming beam momentum. Our energy is purely determined by the dE/dx energy loss of the K^+ in the target and B4.

Given a K^+entering the target, as it traverses the target, it may undergo any of these processes[1]

- dE/dx energy loss $P_{dedx}(E)$,

[1] E is the K^+ energy at the specific point in the target. It is also equivalent to the interaction energy for the processes discussed.

- kaon decay $P_{decay}(E)$,
- CEX $P_{cex}(E)$, and
- elastic and inelastic scattering, $P_{scat}(E)$.

The fate of the K^+ at any point in the target ultimately depends on the probabilities of the processes listed above.

The CEX spectrum shown in Fig. 4.16 is a measure of $P_{cex}(E)$ at each interaction energy. The normalization would be all K^+'s with energy E in the target. Based on statement (2) above, each energy E will have an intrinsic target z distribution (similar to Fig. 4.18) dependent on the incident K^+ energy distribution. We take as our incident K^+ energy distribution the whole $K_{\mu 2}$ sample from the 1997 with 670 MeV/c beam momentum. Since these kaons are known to have decayed at rest, they will only undergo dE/dx energy loss in the target. The task of determining the number of K^+'s with energy E is done by a kaon transport code. The code basically puts a kaon into the target and propagates the kaon until it comes to rest. During the propagation phase, the kaon energy at different target positions is recorded. From this record, we can easily count the total number of kaons with a certain energy E. A description of the code comes in Section 6.1.

Once the flux normalization is known, the cross-section can be calculated using Equation 5.1. There are two problems associated with the use of this equation in the analysis, namely: (i) the equation is only valid for thin target and (ii) the definition of x in our experiment; both consequences of statement (1). The "advantage" in this setup is that the dE/dx energy loss in our thick target has actually allowed us to perform five separate cross-section measurement concurrently. Each energy bin represents a transmission experiment with kaon beam at the energy E_i and target thickness x_i. Based on the energy binning carried out, we defined the target thickness at each energy to be

$$x = R(E_{max}) - R(E_{min}) \tag{6.1}$$

where E_{max} is the upper bound energy of the bin, E_{min} is the lower bound, and R is the corresponding range at those energies. The parameters in the five experiments are listed in Table 6.1.

Energy, MeV	x, cm
10	0.262
30	0.710
50	1.16
70	1.57
90	1.99

Table 6.1: Target thickness x used in cross-section calculation for each energy bin.

Cut	N(passed)
Setup	43585
IC bit	43511
STLAY	40309
RSHEC	38593
TRKTIM	38593
UTC/RANGE	37557
Delco bit	31745
TARGET	31276
COS3D	30619
Offline Delco	26111
BEAM	20949
$N_{K_{\mu 2}}$	20949

Table 6.2: $K_{\mu 2}$ event selection for 1997 runs with 670 MeV/c momentum. This sample is also used to generate the B4-Ek calibration curve.

6.1 Kaon Transport Code

Selection of $K_{\mu 2}$ is done by applying cuts listed in Table 6.2. The events derived from these cuts consisted purely of stopped kaons. The acceptance factors for the $K_{\mu 2}$ selection will be calculated later. The stopping position (tgz) and the target energy deposited (Ek) for the $K_{\mu 2}$ events are skimmed out to a file which serves as the incident kaon beam distribution. A schematic of the code is shown in Fig. 6.1.

The transport code is merely a simple Monte Carlo program that attempts to simulate the passage of K^+ through the target and extract the energy-range spectrum for that K^+. Its input parameter is the K^+'s energy spectrum derived from the $K_{\mu 2}$ sample. During its propagation into the target, the K^+ must first deposit a minimum

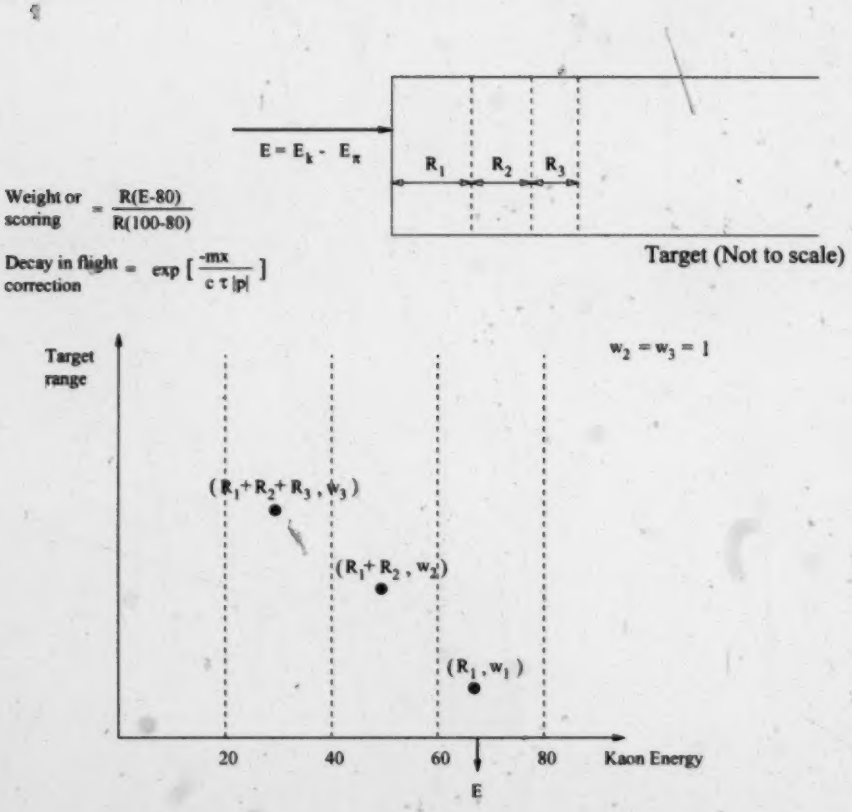

Figure 6.1: Schematic on the transport code of K^+ in the target.

amount of energy before it satisfies the trigger. This is the target sum (TTSum) requirement that constitute the KBeam trigger. Once the K^+ deposited that amount of energy, it will just traverse the target until it stops. Presented below is a detailed example on the working of the code.

Assuming an incoming kaon with total target energy $E_k = 100$ MeV, we will propagate the kaon through the target until it loses all its energy in the target. But first we need to determine the threshold energy the kaon must deposit in order to pass the trigger. The TTSum is an analog sum of the target energy deposited with a threshold of 20 MeV. Since the CEX event is prompt, the online trigger will not be able to distinguish the kaon and pion fibers from the timing information[2]. Hence, included in the target energy is also the pion energy lost in the fibers. To clarify the implication of this point, we will use the 100 MeV kaon as an example. The kaon loses 2 MeV in the target and thus charge exchanges at 98 MeV. The pions resulting from the K^0_S decay deposited 10 MeV in the target, giving us a total of 12 MeV in TTSum. This event will be lost since the TTSum is not satisfied. One has to subtract off the energy contribution from the pion fibers to get the true kaon energy threshold. Since we are interested in the two-track decay of K^0_S, we need to know the energy loss by the two pions in the target. An empirical measurement is performed by simply looking at energy sum of both pion tracks as shown in Fig. 6.2. Taking the mean pion energy loss to be at 14 MeV, the kaon threshold is thus 6 MeV or the starting energy of the K^+ is $E = E_k - E\pi = 100 - 14 = 86$ MeV.

This kaon is then assigned a count or score according to

$$w_i = \frac{R(E) - R(E_{min})}{R(E_{max}) - R(E_{min})} \tag{6.2}$$

where each term has the same meaning as in Equation 6.1, and i is the index for each bin. The scoring system is a result of our definition of x for each energy bin. Basically, the scoring is to account for the number of kaons at a certain energy, E. After travelling $R_1 = 0.523$ cm, the kaon would have lost 6 MeV of energy and counted as $w_1 = 0.263$ in the $80 - 100$ MeV bin. At this point, the kaon becomes an incident particle in the 70 MeV experiment (or the $60 - 80$ MeV bin). Then the kaon will lose another 20 MeV after travelling $R_2 = 1.574$ cm in the target, with scoring $w_2 = 1$ in that bin. This procedure is repeated until the kaon comes to rest.

A decay-in-flight correction needs to be applied for every kaon that we propagate

[2]The fiber classification can be done properly in the offline analysis.

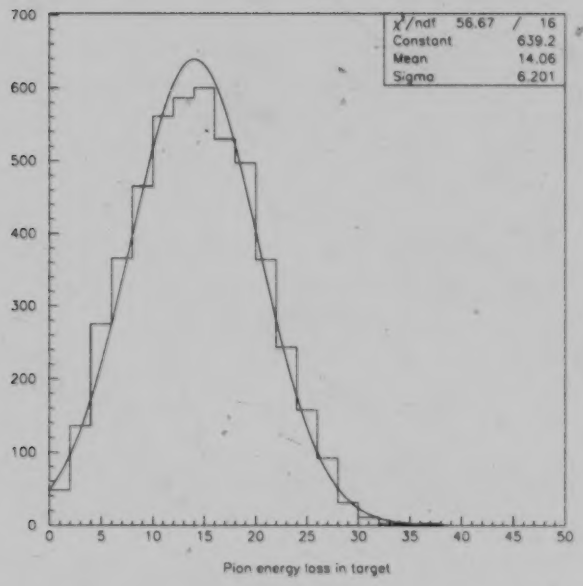

Figure 6.2: Two pion energy loss in the target.

simply because any in-flight kaon before decaying can participate in the CEX interaction. Since our sample of $K_{\mu 2}$ consisted only of stopped kaons, we have to recover the kaons lost to the trigger when they decayed in-flight in the target. Hence the in-flight correction factor is

$$\mathrm{DIF} = w \times \exp\left(\frac{-M_k \Delta x}{c\tau\sqrt{2M_k E + E^2}}\right) \tag{6.3}$$

We can then construct a grid as shown in Fig. 6.3. The target-z axis merely allows us to apply the correction term A_{tgz}. The CEX data plotted in this manner is shown in Fig. 6.4.

Range, cm	10.0	30.0	50.0	70.0	90.0
19.0	110	90	24	4	0
17.0	420	357	138	18	0
15.0	1510	906	486	96	3
13.0	3344	3000	1424	446	26
11.0	5640	5198	3390	1062	108
9.0	9071	7732	6668	3518	337
7.0	9088	10672	8872	6064	1061
5.0	8373	9750	11568	11204	2964
3.0	4145	5318	10373	13626	5406
1.0	827	1670	4532	6894	4877

Energy, MeV

Figure 6.3: Target z-energy distribution for $K_{\mu 2}$. This provides the kaon flux normalization for the cross-section calculation.

6.2 f_s Calculation

Now we need to account for the acceptances for these $K_{\mu 2}$ events. The different factors needed are all summarized in Tables 6.3 and 6.4. The target z biasing effect is corrected using the description in Section 5.1.2.

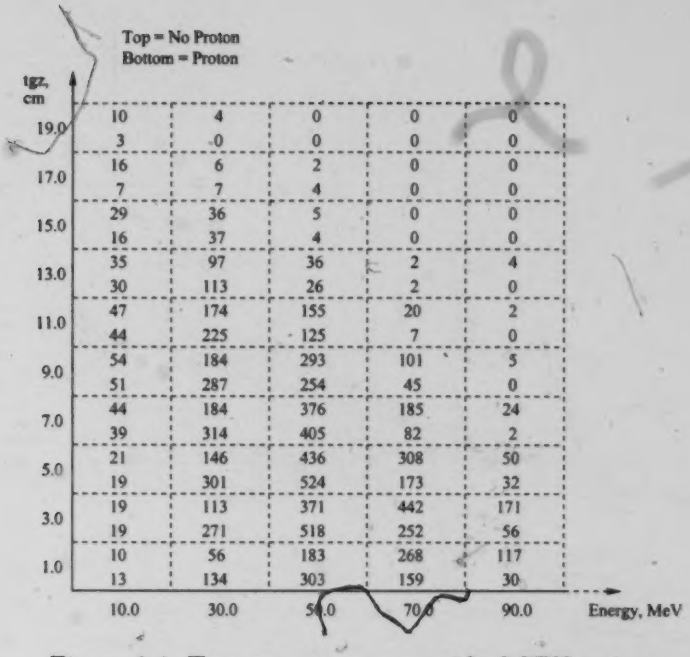

Figure 6.4: Target range-energy grid of CEX events.

Cut	N(passed)	Acceptance
	49998	
T·2	22741	0.455
$\geq$ Layer 19	18838	0.828
A^{trig}		0.377±0.002
STLAY	18498	0.982
UTC/RANGE	18487	0.999
TARGET	18452	0.998
$A_{k\mu 2}$	0.980±0.001	
COS3D	18153	0.984
A^{cos3d}		0.984±0.001

Table 6.3: Trigger and COS3D acceptance factor for $K_{\mu 2}$ from UMC.

Cut	N(passed)	Acceptance
ERD > 100 MeV	29968	
IC bit	29937	0.999
STLAY	28758	0.961
RSHEX	27757	0.965
TRKTIM	27757	1.000
UTC/RANGE	27177	0.979
Delco bit	23552	0.867
TARGET	23267	0.988
A^{recon}		0.776±0.002
1.5σ R,E,P, cut	18580	
Offline Delco	15946	0.858
BEAM	13041	0.818
A_{rest}		0.702±0.004

Table 6.4: Acceptance of the reconstruction cuts.

Energy, MeV	f_s
10	1.5159
30	1.5931
50	1.5307
70	1.5303
90	0.5114

Table 6.5: Kaon flux normalization factor, f_s, at each energy.

With all the acceptance factors in hand, the normalization factor , f_s, for each energy bin is calculated using:

$$\begin{aligned} f_s &= \frac{N(K_{\mu 2})}{KB_{live} \cdot BR} \cdot \mathrm{A}^{-1} \\ &= \frac{N(K_{\mu 2})}{KB_{live} \cdot BR} \cdot \text{prescale} \cdot \left(\mathrm{A}^{\text{trig}} \cdot \mathrm{A}^{\text{cos3d}} \cdot \mathrm{A}^{\text{recon}} \cdot \mathrm{A}^{\text{rest}}\right)^{-1} \end{aligned} \tag{6.4}$$

where $N(K_{\mu 2})$ is the total number of K^+'s scored in the energy bin; prescale = 999440; $KB_{live} = 2.185 \times 10^{11}$; and BR = 0.635. The f_s values are given in Table 6.5.

Chapter 7

Conclusions

7.1 Cross-Section Calculation

With all the acceptances and flux normalization for each energy bin at hand, we can proceed to calculate the cross-sections. Using Equation 5.1 and 5.2, the cross-section for the two different hypothesses are calculated and shown in Table 7.1. The two hypotheses provide an upper and lower bound on the CEX cross-section values measured by this experiment. Listed also are the average cross-section values at each energy. The systematic error is defined to be the difference between the average σ and the σ from the proton or no-proton hypothesis.

	σ, mb		
E_{int}, MeV	Without Proton	With Proton	Mean Value
10	6.1±0.5	6.2±0.6	6.2±0.1±0.6
30	9.9±0.8	14.7±0.9	12.3±2.4±0.9
50	17.8±1.2	21.2±1.3	19.5±1.7±1.3
70	15.8±1.1	13.5±1.2	14.6±1.1±1.2
90	16.7±1.5	11.9±1.1	14.3±2.4±1.3

Table 7.1: CEX cross-section for the proton and no-proton hypotheses. Given also is the mean value between the two hypotheses.

E_{int}, MeV	σ, mb		
	Without Proton	With Proton	Mean Value
20	8.8±1.1	12.3±1.4	10.6±1.2
60	17.7±1.8	18.1±1.4	17.9±1.6
80	15.9±1.8	14.8±1.5	15.4±1.6

Table 7.2: CEX cross-section for a 40 MeV bin size.

E_{int}, MeV	σ, mb		
	Without Proton	With Proton	Mean Value
5	5.6±0.7	6.4±0.8	6.0±0.8
15	4.9±0.7	5.0±0.8	5.0±0.8
25	8.1±1.2	8.7±1.3	8.4±1.2
35	10.2±1.1	17.6±1.8	13.9±1.4
45	15.8±1.4	21.8±2.2	18.8±1.8
55	16.3±1.6	12.0±1.6	14.2±1.6
65	16.2±1.7	14.5±1.4	15.4±1.6
75	14.6±1.6	14.1±1.1	14.4±1.4
85	15.6±1.6	12.7±1.3	14.2±1.4
95	15.2±1.6	14.3±1.0	14.8±1.3

Table 7.3: CEX cross-section values for a 10 MeV bin size.

7.2 Systematic Errors

7.2.1 Energy Binning Effect

The events are binned according to the calculated interaction energy. We have used a 20 MeV bin in this analysis. If the results are stable, varying the bin sizes should not affect the cross-section measurement. Here we will study the effect on the results using a finer bin size (10 MeV) and a broader bin size (40 MeV). The results are summarized in Table 7.2 and 7.3.

7.2.2 Energy Shifting

In deriving the kaon flux normalization, we have taken the mean pion energy loss of 14 MeV to define the kaon threshold. Fig. 6.2 has an approximate 6 MeV spread in the pion energy loss. Any change in the pion energy loss will be reflected in the

	20 MeV shift		8 MeV shift	
E_{int}, MeV	W/O Proton	With Proton	W/O Proton	With Proton
10	6.0±0.5	6.0±0.6	6.8±1.0	6.7±0.8
30	9.7±0.7	12.1±0.8	11.3±1.1	15.7±1.2
50	17.5±1.6	19.3±1.4	16.8±1.3	21.6±1.3
70	18.1±1.6	16.2±1.4	15.4±0.9	12.3±1.1
90	17.9±1.6	17.8±1.6	17.3±1.1	10.6±1.3

Table 7.4: CEX cross-section with different kaon threshold energy

Description	Error
Binning Effect	2 mb
Energy Shift	1 mb
Scattering Effect	1 mb
Resolution Effect	5 mb

Table 7.5: List of systematic errors and their contribution to the cross section values

kaon flux normalization. To study how the cross section changes with this term, we have redone the normalization at 20 MeV and 8 MeV. The results are summarized in Table 7.4.

7.2.3 Kaon Scattering

When we constructed the normalization grid, the only correction term we applied is the decay-in-flight component. We have not included the flux reduction caused by elastic or inelastic scattering of the K^+'s in the target. Failure to account for this factor leads to an underestimation of the kaon flux, particularly in the higher energy bin. Generally, a 6% effect is expected from this factor based on GEANT simulations done in the $\pi^+\nu\bar{\nu}$ studies. For now, we will assert this 6% as a systematic error in our cross section values.

7.3 Discussion

The only experimental data in this energy regime is the K^+-deuterium CEX from Slater *et al.*. That experiment obtained a cross section of σ_D = 2.7 mb at 100±13

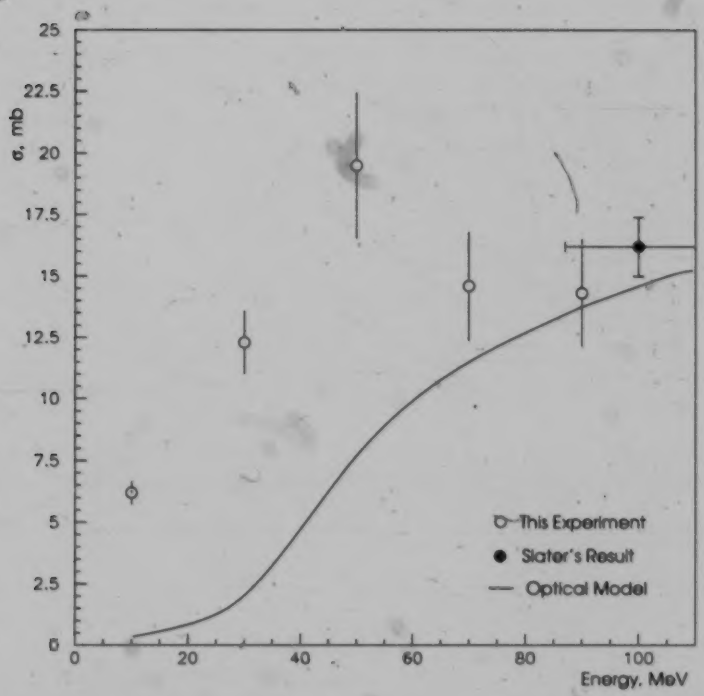

Figure 7.1: Experimental CEX cross section values. The values are compared with Slater's result and optical model prediction (solid curve). Discrepancies at low energies are attributed to resolution effect.

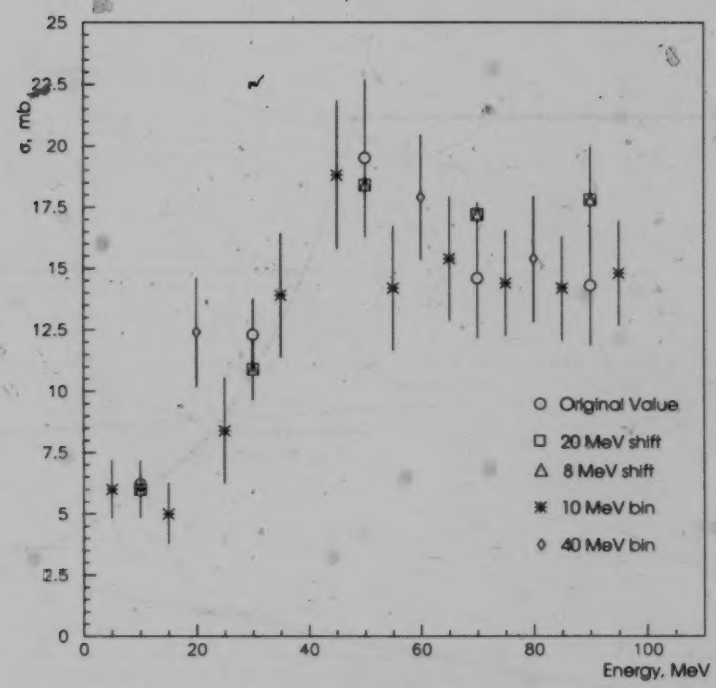

Figure 7.2: Cross section values for the systematic error studies.

MeV [32]. Assuming that ^{12}C consists of six pseudo-deuterons, the K^+-^{12}C CEX cross section is $\sigma_C = 6 \times 2.7 = 16.2$ mb. Both hypotheses gave consistent results at the 90 MeV measurement. Based on conventional optical model calculation, σ_C will be less than 16.2 mb due to the nuclear shadowing effect. Recall from Chapter 2 that results from kaon-nucleus scattering are above the optical model prediction. The increase in cross-section is thought to be due to non-conventional phenomenon like nuclear swelling. Hence, the value of σ_C is probably a slightly better estimate than the optical model prediction.

Fig. 7.1 shows the plot of the experimental values, Slater's result and the theoretical CEX cross section curve. The spectrum is flat down to the 30 MeV point. Though no data should exist below the 20 MeV (the CEX threshold), we still obtained a 6.0 mb cross section. This number gives an indication of the detector resolution. Only a small variation in cross section is observed for the 10 MeV bin. Due to its low energy, events in this bin should consist mainly of the no-proton channel. Even if a proton is emitted, saturation effects should render it unobservable. Therefore, the same result is expected for both scenarios.

Due to Coulomb effect, the cross section can be seen to drop off quite rapidly at lower energies. The experimental values certainly do not follow the theoretical curve. The reader should be reminded that resolution effect is not removed from the results. Hence, the cross section values we obtained here are not the absolute cross section, rather is a convolution of the cross section and the detector resolution function. Untangling this resolution function will be a future work. For now we attributed a 6 mb systematic error for this effect.

In general, the proton energy correction tends to push the events from the higher energy bin (90 and 70 MeV) to the lower energy bin. The no-proton hypothesis does give a flat spectrum whereas the proton hypothesis has a lower cross section in the high energies but a high cross section in the low energies. This seems to imply that the CEX interaction favors the no-proton channel. The proton hypothesis is a correction "forced" upon all the events, hence events with no proton emission are being downshifted in energy while those with proton emission will be given the correct energy. In the case where a bulk of the events consisted of the no-proton channel, the proton energy correction will lead to an overestimation on the cross section in the lower energies, as observed in Table 7.1. Despite this evidence for the no-proton channel, our inability to decouple the proton events from the no-proton events forced us to suffer a 2 mb systematic uncertainty in almost all our measurements.

When a wider binning is used, the event contamination from the different channels is slightly smoothed out. When a finer binning is performed, the variation tends to be a bit more noticeable. The binning effect introduces an systematic uncertainty of 1 mb to our measurement. Then there is the effect of the energy shift in the flux normalization. The spread in the pion energy loss introduces another 2 mb of systematic errors into the high energy measurement. Results for the different studies are summarized in Table 7.5. Comparisons between the studies and the results are shown in Fig. 7.2.

7.4 The Future

Although E787 never intended to perform a CEX cross section measurement, we have been able to extract the low energy cross section values. However, the cross section results obtained from this data have quite substantial systematic errors. Meanwhile the DAΦNE facility at Frascati, Italy has begun operation. Being a ϕ meson factory, it is an excellent source of monochromatic charged kaons. The ϕ, produced by e^+e^- collisions, decays at rest to K^+K^- (BR = 49%) with the charged kaons emerging with 127 MeV/c momentum. The machine is expected have a production rate of $1.25\times10^{10} K^{\pm}$ per year. This facility has the unique opportunity to explore the kinematic region (90 MeV/c – 120 MeV/c) for kaon-nucleus scattering [33]. Hopefully, results from this facility would provide answers to the nuclear swelling phenomenon observed in kaon-nucleus scattering data.

Bibliography

[1] P. Bergbusch, Private Communication, Result to be published

[2] M. Kobayashi and T, Maskawa, Prog. Theor. Phys. **49**, 652 (1973)

[3] L. Wolfenstein, Phys. Rev. Lett. **51**, 1945 (1983)

[4] Eur. Phys. J. **C3**, 103 (1998)

[5] G.Buchalla and A.J. Buras, Nucl. Phys. **B412**, 106 (1994)

[6] W.J. Marciano and Z. Parsa, Phys. Rev. D **53**, R1 (1996)

[7] G.Buchalla and A.J. Buras, TUM-HEP-280/97, hep-ph/9707243

[8] A.J. Buras and R. Fleisher, TUM-HEP-275-97, hep-ph/9704376

[9] J.S. Hagelin and L.S. Littenberg, Prog. Part. Nucl. Phys. **23**, 1 (1989)

[10] D. Rein and L.M. Sehgal, Phys. Rev. D **39**, 3325 (1989)

[11] A.J. Buras, M.E. Lautenbacher, and G. Ostermaier, Phys. Rev. D **50**, 3433 (1994)

[12] C.B. Dover and G.E. Walker, Phys. Rep. **89**, 1 (1982)

[13] C.B. Dover and P.J. Moffa, Phys. Rev. C **16**, 1087 (1977)

[14] A.S. Carroll *et al.*, Phy. Rev. Lett. **37**, 806 (1976)

[15] B.R. Martin, Nucl. Phys. **B94**, 413 (1975).

[16] R. Weiss *et al.*, Phys. Rev. C **49**, 2569 (1994)

[17] R. Krauss *et al.*, Phys. Rev. C **46**, 655 (1992)

[18] P.B. Siegel, W.B. Kaufmann, and W.R. Gibbs, *Phys. Rev. C* **30**, 1256 (1984).

[19] W.B. Kaufmann and W.R. Gibbs, Phys. Rev. C **28**, 1286 (1983).

[20] W.B. Kaufmann and W.R. Gibbs, Phys. Rev. C **40**, 1729 (1989).

[21] G.E. Brown, C.B. Dover, P.B. Siegel, and W. Weise, Phys. Rev. Lett. **60**, 2723 (1988)

[22] A.B. Migdal *et al,*, Phys. Rep. **192**, 181 (1990)

[23] S.V. Akulinichev, Phy. Rev. Lett. **68**, 290 (1992)

[24] M.L. Goldberger and K.M. Watson, *Collision Theory* (John Wiley, New York, 1964)

[25] O.D Dalkarov and V.A. Karmanov, Nucl. Phys. **B445**, 579 (1985)

[26] R.A. Arndt and L.D Roper, Phys. Rev. D **46**, 961 (1992)

[27] Eliot Friedman, Private Communication.

[28] J. Stone, TechNote 326, (Unpublished)

[29] P. Bergbusch, TechNote 365, (Unpublished)

[30] C. Wilkin, Nucl. Phys. **B62**, 61 (1973)

[31] O. Meirav *et al.*, Phys. Rev C **36**, 1066 (1987)

[32] W. Slater *et al.*, Phys. Rev. Lett. **7**, 378 (1961)

[33] P.M. Gensini, Second DAΦNE Physics Handbook Vol. II, 735 (1995)

Appendix A

UMC Performance

Features of UMC are tailored mostly to the needs of the $\pi^+\nu\bar{\nu}$ analysis. Since the $\pi^+\nu\bar{\nu}$ analysis deals with π^+, UMC provides very reliable simulation of the π^+ in the RS. This is why all correction terms related to π^+ in this analysis are dealt with using UMC. However, π^- simulation is not a feature found in the UMC program. Therefore one has to resort to the CEX data itself to correct for the nuclear interaction process.

To test the reliability of UMC, CEX events generated are compared with the data. Shown in Fig. A.1 and Fig. A.2 are comparisons of the RS range distributions between UMC and data for π^- and π^+. The range distributions for π^- at all three momenta do not replicate the features seen in the data. Instead the simulated π^- events yielded a clean distribution since they can only undergo dE/dx energy loss in the RS. As for the π^+, there is a good agreement between UMC events and data. In fact, UMC even managed to simulate the onset Δ resonant at 270 MeV/c.

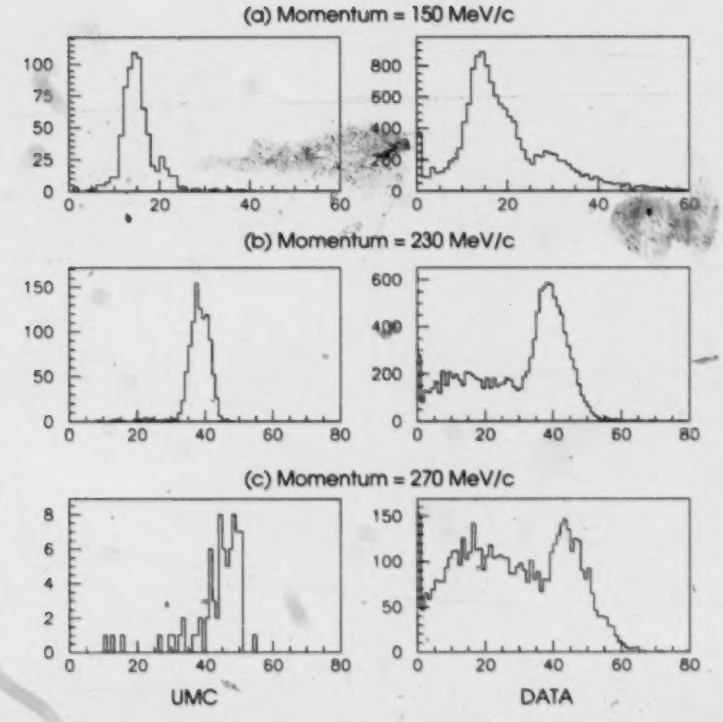

Figure A.1: Comparison of RS range distributions of π^- at momenta 165, 230, 270 MeV/c between UMC and data. UMC only simulated the dE/dx energy loss in the RS and failed to simulate nuclear interaction processes the π^- might undergo.

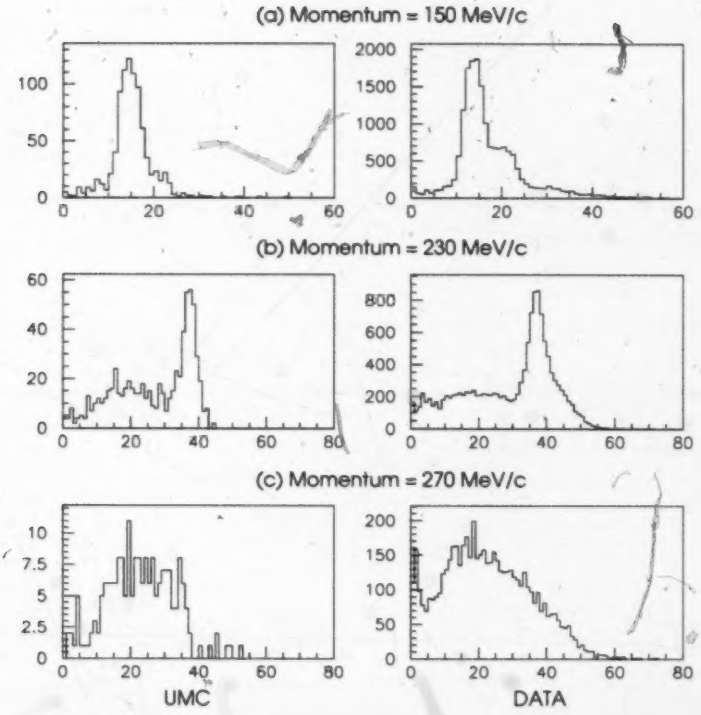

Figure A.2: Comparison of RS range distributions of π^+ at momenta 150, 230, 270 MeV/c between UMC and data. UMC is able to simulate the π^+ nuclear interaction reliably. At 270 MeV/c, the prominent Δ resonant is observed for both UMC and data.